Asteroid Measurements at Millimeter Wavelengths with the South Pole Telescope

P. M. Chichura[1,2], A. Foster[3], C. Patel[4], N. Ossa-Jaen[5], P. A. R. Ade[6], Z. Ahmed[7,8], A. J. Anderson[2,9], M. Archipley[10,11], J. E. Austermann[12,13], J. S. Avva[14], L. Balkenhol[15], P. S. Barry[2,16], R. Basu Thakur[2,17], J. A. Beall[12], K. Benabed[18], A. N. Bender[2,16], B. A. Benson[2,9,19], F. Bianchini[7,15,20], L. E. Bleem[2,16], F. R. Bouchet[18], L. Bryant[21], K. Byrum[16], J. E. Carlstrom[1,2,16,19,21], F. W. Carter[2,16], T. W. Cecil[16], C. L. Chang[2,16,19], P. Chaubal[15], G. Chen[22], H. C. Chiang[23,24], H.-M. Cho[8], T-L. Chou[1,2], R. Citron[22], J.-F. Cliche[25], T. M. Crawford[2,19], A. T. Crites[2,19,26,27], A. Cukierman[7,8,20], C. M. Daley[10], E. V. Denison[12], K. Dibert[2,19], J. Ding[28], M. A. Dobbs[25,29], D. Dutcher[1,2], W. Everett[30], C. Feng[31], K. R. Ferguson[32], J. Fu[10], S. Galli[18], J. Gallicchio[2,33], A. E. Gambrel[2], R. W. Gardner[21], E. M. George[14,34], N. Goeckner-Wald[7,20], R. Gualtieri[16], S. Guns[14], N. Gupta[15], R. Guyser[10], T. de Haan[35], N. W. Halverson[13,30], A. H. Harke-Hosemann[10,16], N. L. Harrington[14], J. W. Henning[2,16], G. C. Hilton[12], E. Hivon[18], G. P. Holder[4], W. L. Holzapfel[14], J. C. Hood[2], D. Howe[22], J. D. Hrubes[22], N. Huang[14], J. Hubmayr[12], K. D. Irwin[7,8,20], O. B. Jeong[14], M. Jonas[9], A. Jones[22], T. S. Khaire[28], L. Knox[36], A. M. Kofman[37], M. Korman[3], D. L. Kubik[9], S. Kuhlmann[16], C.-L. Kuo[7,8,20], A. T. Lee[14,38], E. M. Leitch[2,19], D. Li[8,12], A. Lowitz[2], C. Lu[4], D. P. Marrone[39], J. J. McMahon[1,2,19], S. S. Meyer[1,2,19,21], D. Michalik[22], M. Millea[14], L. M. Mocanu[2,19,40], J. Montgomery[25], C. Corbett Moran[41], A. Nadolski[10], T. Natoli[2,19], H. Nguyen[9], J. P. Nibarger[12], G. Noble[25], V. Novosad[28], Y. Omori[7,20], S. Padin[2,17], Z. Pan[1,2,16], P. Paschos[21], S. Patil[15], J. Pearson[28], K. A. Phadke[10], C. M. Posada[28], K. Prabhu[36], C. Pryke[42], W. Quan[1,2], A. Rahlin[2,9], C. L. Reichardt[15], D. Riebel[22], B. Riedel[21], M. Rouble[25], J. E. Ruhl[3], B. R. Saliwanchik[43,44], J. T. Sayre[30], K. K. Schaffer[2,21,45], E. Schiappucci[15], E. Shirokoff[2,19], C. Sievers[22], G. Smecher[46], J. A. Sobrin[1,2], A. Springmann[47], A. A. Stark[48], J. Stephen[21], K. T. Story[7,20], A. Suzuki[38], C. Tandoi[10], K. L. Thompson[7,8,20], B. Thorne[36], C. Tucker[6], C. Umilta[4], L. R. Vale[12], T. Veach[49], J. D. Vieira[4,10,11], G. Wang[16], N. Whitehorn[32,50], W. L. K. Wu[2,7,8], V. Yefremenko[16], K. W. Yoon[7,8,20], and M. R. Young[27]

[1] Department of Physics, University of Chicago, 5640 South Ellis Avenue, Chicago, IL, 60637, USA; pchichura@uchicago.edu
[2] Kavli Institute for Cosmological Physics, University of Chicago, 5640 South Ellis Avenue, Chicago, IL, 60637, USA
[3] Department of Physics, Case Western Reserve University, Cleveland, OH, 44106, USA
[4] Department of Physics, University of Illinois Urbana-Champaign, 1110 West Green Street, Urbana, IL, 61801, USA
[5] Department of Physics, University of Redlands, 1267 East Colton Ave, Redlands, CA, 92374, USA
[6] School of Physics and Astronomy, Cardiff University, Cardiff CF24 3YB, UK
[7] Kavli Institute for Particle Astrophysics and Cosmology, Stanford University, 452 Lomita Mall, Stanford, CA, 94305, USA
[8] SLAC National Accelerator Laboratory, 2575 Sand Hill Road, Menlo Park, CA, 94025, USA
[9] Fermi National Accelerator Laboratory, MS209, P.O. Box 500, Batavia, IL, 60510, USA
[10] Department of Astronomy, University of Illinois at Urbana-Champaign, 1002 West Green Street, Urbana, IL, 61801, USA
[11] Center for AstroPhysical Surveys, National Center for Supercomputing Applications, Urbana, IL, 61801, USA
[12] NIST Quantum Devices Group, 325 Broadway Mailcode 817.03, Boulder, CO, 80305, USA
[13] Department of Physics, University of Colorado, Boulder, CO, 80309, USA
[14] Department of Physics, University of California, Berkeley, CA, 94720, USA
[15] School of Physics, University of Melbourne, Parkville, VIC 3010, Australia
[16] High-Energy Physics Division, Argonne National Laboratory, 9700 South Cass Avenue, Argonne, IL, 60439, USA
[17] California Institute of Technology, 1200 East California Boulevard., Pasadena, CA, 91125, USA
[18] Institut d'Astrophysique de Paris, UMR 7095, CNRS & Sorbonne Université, 98 bis boulevard Arago, F-75014 Paris, France
[19] Department of Astronomy and Astrophysics, University of Chicago, 5640 South Ellis Avenue, Chicago, IL, 60637, USA
[20] Department of Physics, Stanford University, 382 Via Pueblo Mall, Stanford, CA, 94305, USA
[21] Enrico Fermi Institute, University of Chicago, 5640 South Ellis Avenue, Chicago, IL, 60637, USA
[22] University of Chicago, 5640 South Ellis Avenue, Chicago, IL, 60637, USA
[23] Department of Physics, McGill University, 3600 Rue University, Montreal, Quebec H3A 2T8, Canada
[24] School of Mathematics, Statistics & Computer Science, University of KwaZulu-Natal, Durban, South Africa
[25] Department of Physics and McGill Space Institute, McGill University, 3600 Rue University, Montreal, Quebec H3A 2T8, Canada
[26] Dunlap Institute for Astronomy & Astrophysics, University of Toronto, 50 St George Street, Toronto, ON, M5S 3H4, Canada
[27] Department of Astronomy & Astrophysics, University of Toronto, 50 St George St, Toronto, ON, M5S 3H4, Canada
[28] Materials Sciences Division, Argonne National Laboratory, 9700 South Cass Avenue, Argonne, IL, 60439, USA
[29] Canadian Institute for Advanced Research, CIFAR Program in Gravity and the Extreme Universe, Toronto, ON, M5G 1Z8, Canada
[30] CASA, Department of Astrophysical and Planetary Sciences, University of Colorado, Boulder, CO, 80309, USA
[31] Department of Astronomy, University of Science and Technology of China, 96 Jinzhai Road, Hefei, Anhui, 230026, People's Republic of China
[32] Department of Physics and Astronomy, University of California, Los Angeles, CA, 90095, USA
[33] Harvey Mudd College, 301 Platt Boulevard, Claremont, CA, 91711, USA
[34] European Southern Observatory, Karl-Schwarzschild-Strasse 2, D-85748 Garching bei München, Germany
[35] High Energy Accelerator Research Organization (KEK), Tsukuba, Ibaraki 305-0801, Japan
[36] Department of Physics & Astronomy, University of California, One Shields Avenue, Davis, CA 95616, USA
[37] Department of Physics & Astronomy, University of Pennsylvania, 209 S 33rd Street, Philadelphia, PA 19064, USA
[38] Physics Division, Lawrence Berkeley National Laboratory, Berkeley, CA, 94720, USA
[39] Steward Observatory, University of Arizona, 933 North Cherry Avenue, Tucson, AZ 85721, USA
[40] Institute of Theoretical Astrophysics, University of Oslo, P.O.Box 1029 Blindern, NO-0315 Oslo, Norway
[41] TAPIR, Walter Burke Institute for Theoretical Physics, California Institute of Technology, 1200 E California Blvd, Pasadena, CA, 91125, USA
[42] School of Physics and Astronomy, University of Minnesota, 116 Church Street S.E. Minneapolis, MN, 55455, USA
[43] Physics Department, Center for Education and Research in Cosmology and Astrophysics, Case Western Reserve University, Cleveland, OH, 44106, USA
[44] Department of Physics, Yale University, P.O. Box 208120, New Haven, CT, 06520, USA
[45] Liberal Arts Department, School of the Art Institute of Chicago, 112 S Michigan Avenue, Chicago, IL, 60603, USA
[46] Three-Speed Logic, Inc., Victoria, B.C., V8S 3Z5, Canada

[47] Department of Planetary Sciences, University of Arizona, 1629 East University Boulevard, Tucson, AZ, 85722, USA
[48] Harvard-Smithsonian Center for Astrophysics, 60 Garden Street, Cambridge, MA, 02138, USA
[49] Space Science and Engineering Division, Southwest Research Institute, San Antonio, TX, 78238, USA
[50] Department of Physics and Astronomy, Michigan State University, East Lansing, MI, 48824, USA

Abstract

We present the first measurements of asteroids in millimeter wavelength data from the South Pole Telescope (SPT), which is used primarily to study the cosmic microwave background (CMB). We analyze maps of two $\sim$270 deg^2 sky regions near the ecliptic plane, each observed with the SPTpol camera $\sim$100 times over 1 month. We subtract the mean of all maps of a given field, removing static sky signal, and then average the mean-subtracted maps at known asteroid locations. We detect three asteroids—(324) Bamberga, (13) Egeria, and (22) Kalliope—with signal-to-noise ratios (S/N) of 11.2, 10.4, and 6.1, respectively, at 2.0 mm (150 GHz); we also detect (324) Bamberga with an S/N of 4.1 at 3.2 mm (95 GHz). We place constraints on these asteroids' effective emissivities, brightness temperatures, and light-curve modulation amplitude. Our flux density measurements of (324) Bamberga and (13) Egeria roughly agree with predictions, while our measurements of (22) Kalliope suggest lower flux, corresponding to effective emissivities of 0.64 ± 0.11 at 2.0 and < 0.47 at 3.2 mm. We predict the asteroids detectable in other SPT data sets and find good agreement with detections of (772) Tanete and (1093) Freda in recent data from the SPT-3G camera, which has $\sim$10$\times$ the mapping speed of SPTpol. This work is the first focused analysis of asteroids in data from CMB surveys, and it demonstrates we can repurpose historic and future data sets for asteroid studies. Future SPT measurements can help constrain the distribution of surface properties over a larger asteroid population.

Unified Astronomy Thesaurus concepts: Asteroids (72); Asteroid surfaces (2209); Millimeter astronomy (1061); Cosmic microwave background radiation (322)

1. Introduction

Astronomers can learn about the evolution of our solar system and its planets by studying the physical properties of asteroids (Michel et al. 2015). Typically, astronomers observe asteroids passively at optical and thermal infrared (IR) wavelengths; in these wavelength ranges, the asteroid flux densities are dominated by reflected solar light and thermal emission, respectively. Astronomers also study asteroids actively with radar observations, which detect echo signals to determine physical shape and properties. While astronomers do study asteroids at submillimeter, millimeter, and centimeter wavelengths, such studies are less frequent, despite the feasibility of such measurements having been demonstrated as early as the 1970s (Briggs 1973). These microwave observations provide information that optical, IR, and radar observations cannot. For instance, early observers at microwave wavelengths correctly understood that emission from wavelengths longer than IR originated from multiple wavelengths into the *regolith*, i.e., the unconsolidated rocky surface of the asteroid, depending on regolith composition (Ulich & Conklin 1976; Conklin et al. 1977; Johnston et al. 1982). That is, the regolith becomes more transparent at longer wavelengths, so early observers found they could measure thermal radiation emitted from deeper under the asteroid's surface.

Studies at IR wavelengths suggested that most large asteroids had surface emissivities near unity, yet early observations from submillimeter to centimeter wavelengths measured flux densities much lower than models predicted. These early observers interpreted the lower flux densities as the result of a wavelength-dependent drop in emissivity as large as 25% (Johnston et al. 1982; Webster et al. 1988). At the time,

astronomers interpreted this lower emissivity as an effective emissivity resulting from scattering by grains within the regolith, which would make it harder for photons to escape to the surface (Redman et al. 1992). Astronomers used this interpretation to place constraints on the composition and properties of asteroids' surfaces, and they continued interpreting asteroids in this way for decades, including in some recent studies at these wavelengths that observe emissivity drops as great as 40% (Müller & Barnes 2007; Moullet et al. 2010).

However, there is mounting evidence that this interpretation is incorrect. The European Space Agency's Rosetta is the first solar system spacecraft mission that includes instrumentation able to measure thermal fluxes at IR, submillimeter, and millimeter wavelengths. Rosetta made close approaches to two asteroids, one of which was the large asteroid (21) Lutetia[51] (Gulkis et al. 2012). During the flyby of (21) Lutetia, Rosetta also recorded a decrease in flux at millimeter wavelengths, but more complex modeling suggested that this was due to a large temperature gradient in the outer regolith as opposed to a wavelength-dependent emissivity (Keihm et al. 2012). Later, Keihm et al. (2013) applied their modeling to thermal fluxes of other large asteroids to suggest an altogether new interpretation of the observed decrease in flux at longer wavelengths. They found that the decrease in flux could be explained by emissivities near unity at all wavelengths combined with a significant temperature gradient over depth, with temperatures as much as 50–80 K lower several millimeters below the asteroid's surface.

The new interpretation suggested by Keihm et al. (2013) represents a paradigm shift that would fundamentally alter the way astronomers examine asteroid regolith composition. In order to expand on this work, astronomers need more high-sensitivity measurements of asteroids at submillimeter to centimeter wavelengths, where observations exist for only a handful of

[51] The naming convention of asteroids consists of an object's International Astronomical Union designation number in parentheses followed by its name (if any).

large asteroids. Recently, the Atacama Large Millimeter/ submillimeter Array (ALMA) carried out dedicated studies of asteroids and other small solar system bodies, including asteroids (1) Ceres (Li et al. 2020), (3) Juno (ALMA Partnership et al. 2015), and (16) Psyche (de Kleer et al. 2021), as well as Centaurs and trans-Neptunian objects (Lellouch et al. 2017). Measurements like these at submillimeter to centimeter wavelengths serve an important role in asteroid studies because they lie on the ill-understood boundary between two observable regimes—the highly emissive radiation in IR and the supposedly less emissive radiation in centimeters—and ultimately can improve modeling of surface properties, including thermal inertia and regolith roughness.

Instruments like ALMA can track celestial targets for a short time with high sensitivity, but these instruments are generally facilities that require proposals for use. These facilities receive many observation requests, so studying asteroids comes at a high opportunity cost. However, astronomers can incur no opportunity cost if they repurpose data from other types of observations that happen to include asteroids. Sky surveys at millimeter wavelengths fill this niche and are made frequently using telescopes designed to study the cosmic microwave background (CMB).

In this paper, we show that we can use data from the South Pole Telescope (SPT) to detect asteroids at high signal-to-noise ratios (S/N) at millimeter wavelengths when we average maps of the sky centered on known asteroid locations. By showing this, we demonstrate that historic and future data from CMB experiments can be repurposed for observing asteroids. In Section 2, we describe the SPT and the cameras from which the data in this paper are taken, the specific observations used in this work, and the data processing used in making the single-observation maps used in the asteroid search. In Section 3, we explain the asteroid selection criteria in historic data. In Section 4, we describe how we search for the selected asteroids in our observations. In Section 5, we show the detection of three large asteroids—(324) Bamberga, (13) Egeria, and (22) Kalliope—with the SPTpol camera at 2 mm (150 GHz), as well as (324) Bamberga at 3.2 mm (95 GHz). In Section 6, we discuss these results. In Section 7, we suggest prospects for continuing this analysis on other data sets. We conclude in Section 8.

Although the Planck Collaboration has previously published detections of asteroids in their analysis connecting dust observations to asteroid families (Cremonese et al. 2002; Planck Collaboration et al. 2014) and the Atacama Cosmology Telescope (ACT) collaboration masked asteroids in their search for Planet 9 (Naess et al. 2021), this work represents the first focused analysis of asteroid flux in data from an experiment designed to measure the CMB. With continued analysis, historic and future data measuring the CMB can provide more observations of asteroids at submillimeter and millimeter wavelengths. In particular, scientists can make these measurements using a wealth of data provided by current experiments, such as those on SPT and ACT, as well as upcoming experiments like the Simons Observatory and CMB-S4 (Kosowsky 2003; Abazajian et al. 2016; Simons Observatory Collaboration et al. 2019).

2. Instruments, Observations, Data Processing

The primary results in this work use observations from the SPTpol camera on the SPT, with some proof-of-concept results from the currently installed SPT-3G camera. We provide a brief description of the telescope and both cameras, the method of data collection—particularly as it pertains to the sensitivity to moving objects—and the standard data analysis through the mapmaking step. We describe the post-map processing specific to asteroid detection and characterization in Section 4.

2.1. Telescope and Cameras

The SPT is a millimeter/submillimeter telescope with a 10 m primary mirror, installed at the National Science Foundation Amundsen-Scott South Pole research station. The telescope is physically located approximately 1 km from the geographical South Pole. Since its construction in 2006–2007, the SPT has been used almost exclusively to make deep maps of thousands of square degrees of the southern sky, with the primary science goal of characterizing the primary and secondary CMB anisotropies in intensity and polarization. For more details on the telescope, see Carlstrom et al. (2011) and Padin et al. (2008).

SPTpol was the second camera installed on the telescope, replacing the original SPT-SZ camera in 2012. SPTpol consisted of 1536 feedhorn-coupled, polarization-sensitive superconducting detectors, 1176 sensitive to radiation in a band centered near 2.0 mm (150 GHz) and 360 sensitive to radiation in a band centered near 3.2 mm (95 GHz). Although we refer to these bands as "2.0 mm" and "3.2 mm," the band centers are closer to 2.01 mm (149.3 GHz) and 3.11 mm (96.2 GHz), respectively, for a Rayleigh–Jeans spectrum, like that expected from asteroids. These effective band centers may shift slightly if we consider the drop in effective emissivity described in Section 1, but this shift would only minimally alter measured fluxes and effective emissivities. We can approximate the main lobes of the SPTpol beams or point-spread functions in the two bands by Gaussians with an FWHM equal to roughly $1.'2$ at 2.0 mm and $1.'6$ at 3.2 mm. More details on SPTpol can be found in Austermann et al. (2012) and Bleem et al. (2012).

The SPT-3G camera replaced SPTpol on the telescope in 2017. SPT-3G consists of $\sim$16,000 superconducting detectors configured to observe in three bands, centered at roughly 1.4 mm (220 GHz), 2.0 mm (150 GHz), and 3.2 mm (95 GHz). Each camera pixel is coupled to two (orthogonally polarized) detectors in each of the three bands. The beam FWHM for SPT-3G is similar to that in SPTpol for the two common bands and is roughly $1.'05$ at 1.4 mm. For more details on SPT-3G, see Anderson et al. (2018) and Sobrin et al. (2022).

Both SPTpol and SPT-3G contain polarization-sensitive detectors. Observers might expect to measure the polarization of microwave emissions but only at polarization levels of a few tens of percent (Lagerros 1996). Indeed, recent observations at mm wavelengths have found polarization levels even lower than theory might suggest (de Kleer et al. 2021). Therefore, we expect that any measurements of polarized light from the asteroids considered in this paper would be approximately an order of magnitude weaker than measurements of total intensity. Given the significance at which we ultimately detect unpolarized emission of asteroids considered in this paper, we only use the total intensity information from SPTpol and SPT-3G in this work.

2.2. Observations

The primary results in this work come from observations with the SPTpol camera of two sky regions: "RA13HDEC-25" centered at roughly R.A. 13^h, decl. -25°, and "RA23HDEC-25"

centered at roughly R.A. 23^h, decl. $-25°$. Each field is 2^h wide in R.A. and 10° tall in decl., covering roughly 270 deg^2 each. We note that these are different from the primary SPTpol science field, a 500 deg^2 patch centered at R.A. 0^h, decl. $-57°.5$ (Henning et al. 2018).

From roughly December through March, the primary science field was partially contaminated by the Sun due to telescope sidelobes, so SPTpol was used to conduct a supplementary survey of other fields with relatively low Galactic foreground emission. This supplementary survey is called the SPTpol Extended Cluster Survey (ECS), the details of which can be found in (Bleem et al. 2020, hereafter B20). The ECS covers nearly 2800 deg^2; we concentrate on the two fields mentioned above because of their proximity to the ecliptic plane, as explained in Section 3.

Each of these two fields was observed for roughly 1 month in either 2015 or 2016, on a roughly 2.5 hr cadence, with a $\sim$4 hr pause every $\sim$24 hr for cycling the helium adsorption refrigerator that cools the detectors. The RA23HDEC-25 field was observed from 2015 October 29 to 2015 November 29. The mean position of the Sun during this time was at R. A. 226°.6 and decl. $-17°.2$. The RA13HDEC-25 field was observed for 1 day on 2016 February 13 then from 2016 February 23 through 2016 March 22. The mean position of the Sun during this time was at R.A. 315°.9 and decl. $-4°.2$. Bleem et al. (2020) estimate the final noise level of the two fields to be roughly 30 μK-arcmin at 2.0 mm and 50–60 μK-arcmin at 3.2 mm, corresponding to 1σ point-source sensitivities of roughly 2 and 3 mJy at 2.0 and 3.2 mm, respectively.

In Section 7, we perform a rough validation of predictions for asteroid yield in other surveys using 2020 data from the main SPT-3G science field, a 1500 deg^2 field centered at R.A. 0^h, decl. $-56°$ (a superset of the SPTpol main science field). In 2020 this field was observed from March through November, with an effective cadence of 1–2 days (the full field is split into four subfields, two of which are observed during a given refrigerator cycle—see Guns et al. (2021) for details).

2.3. Data Processing

2.3.1. Time-ordered Data Filtering and Mapmaking

The maps used in this work were originally created for use in the cluster-finding analysis of Bleem et al. (2020). For details of the data processing used to make these maps, we refer the reader to that work; we summarize the basic steps here. For each observation, the time-ordered data (TOD) were subject to quality cuts and several filtering steps, including bandpass filtering to suppress low- and high-frequency noise and common-mode subtraction to suppress atmospheric contamination. The sky location to which each detector was pointed at each time sample was then calculated and binned into 0′.25 pixels in the Sanson–Flamsteed projection. Finally, all time samples from all detectors in a given observing band pointing to a given pixel were averaged with inverse noise weighting to produce the map.

Because of the finite resolution of the telescope and the filtering applied to the TOD, the resulting maps are biased representations of the true sky signal. We can represent both the telescope resolution effect and the effect of the TOD filtering as multiplications in two-dimensional Fourier space, and we refer to these as the beam $B(\boldsymbol{l})$ and the filter transfer function $F(\boldsymbol{l})$, respectively, where $\boldsymbol{l} \in \{l_x, l_y\}$ is the wavenumber

equivalent of the Fourier coordinate system $\{u, v\}$ (i.e., $l_x = 2\pi u$, $l_y = 2\pi v$). The most important TOD filtering steps are (1) a scan-direction high-pass filter that, combined with the azimuth-raster scan strategy and the polar telescope location, results in a map-space x-direction high pass with a cutoff of $l_x = 300$; and (2) a common-mode subtraction across the array at each time step that acts in map space as an isotropic high-pass with a cutoff of roughly $\ell \equiv |\boldsymbol{l}| = 300$.

2.3.2. Calibration

Relative gains across the detector array and between observations are measured using regular observations of the Galactic H II region RCW38 and regular observations of an internal thermal calibration source. As in Bleem et al. (2020), the absolute calibration of the map was derived by comparing the full-season co-added maps with the Planck map of the same field. The SPT-ECS fields were taken at significantly higher levels of atmospheric loading compared to other SPTpol survey data, and the resulting larger change in detector loading with elevation necessitated a further calibration step beyond a constant normalization factor for 3.2 mm data. Although noise in SPTpol data does not in general depend strongly on airmass, the 3.2 mm data required this additional calibration step as the calibration was empirically found to vary significantly with elevation within a field (which is equivalent to decl. for observations from the South Pole). This trend is fit well as a linear function of decl., and Bleem et al. (2020) used the Planck data to fit for and correct this variation across the fields.

Because in this work we aim to measure asteroid flux density on an observation-to-observation basis, we also compare individual observations with Planck data. We find that the single-observation calibration varies significantly less than the noise on the measurement of any asteroid in a single observation, and we ignore this as a source of uncertainty in subsequent analysis. We also repeat the B20 comparison of the full-depth SPTpol maps with Planck data and make small ($\sim$5% level) corrections to the B20 absolute calibration.

The comparison to Planck yields a calibration at angular scales where the CMB temperature anisotropy is strongest (roughly degree scales), and transferring this to a flux density scale requires accurate knowledge of the beam and filtering. We verify our flux density calibration by comparing flux measurements of the source J2258-2758 at 3.2 mm in RA23H-DEC-25 with the value reported in the ALMA Calibrator Source Catalogue.[52] This source is the only source recorded in the catalog during the observation periods of our fields. We found that ALMA's measurement was within $\sim$1 standard deviation of our measurement from five observations near ALMA's observation date. Because we are primarily checking for systematic failures in the beam and filter transfer function estimation, we take the success of the verification at 3.2 mm and in one field to indicate that the flux density calibration chain is likely robust at 2.0 mm and in the other field.

Overall, these calibration steps carry a few systematic uncertainties. Uncertainty in 3.2 mm data from the elevation-dependent recalibration done by Bleem et al. (2020) is around 5.9% (5.5%) for RA13HDEC-25 (RA23HDEC-25). Uncertainty from calibration with Planck data is around 1.4% (2.4%) for RA13HDEC-25 (RA23HDEC-25) in 2.0 mm data and 2.3% (2.0%) for RA13HDEC-25 (RA23HDEC-25) in 3.2 mm data. There is
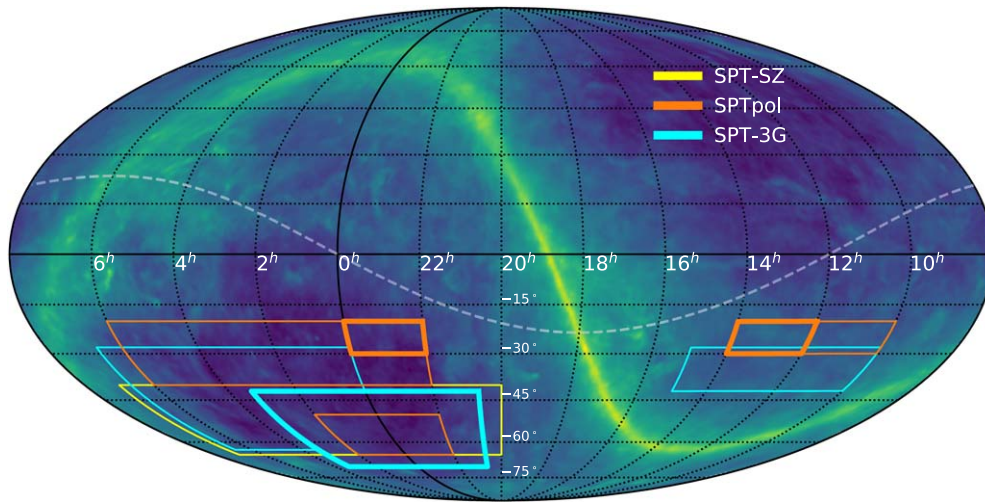
---

[52] https://almascience.nrao.edu/sc/

Figure 1. SPT-SZ, SPTpol, and SPT-3G observation fields plotted on a Mollweide projection of the sky using the equatorial coordinate system. The yellow, orange, and cyan boxes denote the sky regions observed using the SPT, and thicker boxes denote regions analyzed in this paper. The blue-green-yellow color scale represents galactic dust emission at 545 GHz from the Planck Public Data Release 2, with yellow indicating higher emission (Planck Collaboration et al. 2016). The dashed gray line represents the ecliptic plane.

further uncertainty related to the SPTpol beam shape used in filtering maps and converting map units to flux units; this is at most on the scale of a few percent. Added in quadrature, these systematic uncertainties are roughly 6% for the 3.2 mm data and 3% for the 2.0 mm data, which are subdominant to noise fluctuations in observations of the asteroids reported in Section 5.

3. Selecting Asteroids to Examine

Figure 1 shows a map of the Galactic dust emission from the Planck satellite, with the locations of the SPTpol and SPT-3G observation fields and the ecliptic plane superimposed. Galactic emission can obscure measurements of the CMB, so CMB survey designers typically choose observation fields that avoid this emission. The ecliptic plane marks the apparent path of the Sun through the sky over the course of a year, so near it we should find objects in our solar system with low orbital inclination, like most main belt asteroids (MBAs). Thus, we would expect to find more observable asteroids in the fields closest to the ecliptic, and we focus our initial search on those fields: SPTpol ECS fields RA13HDEC-25 and RA23HDEC-25 (detailed in Section 2.2).

To identify observable asteroids, we predict the asteroids' flux densities using standard thermal models. Three such models are commonly employed: the standard thermal model (STM) developed by Lebofsky et al. (1986), the fast rotating model (FRM) developed by Lebofsky & Spencer (1989), and the near-Earth asteroid thermal model (NEATM) developed by Harris (1998). For a review of all three models, we refer the reader to Delbó & Harris (2002). All three models consider thermal equilibrium between incoming solar radiation and outgoing emitted radiation on the surface of an asteroid. The STM considers the case in which an asteroid is not rotating, reaches a maximum temperature at the subsolar point, and radiates only from the dayside. The FRM considers the case in which an asteroid is rotating quickly and reaches a maximum temperature along its hemisphere. The NEATM considers the same case as the STM, except it integrates emission from the asteroid's visible surface as opposed to using empirical scaling with solar phase angle. The models generally take the

following parameters: solar distance, Earth distance, solar phase angle, bond albedo, emissivity, and *beaming parameter*. The beaming parameter was originally included to account for an effect called *infrared beaming* in which thermal emission is greater from a rough surface when viewed at small phase angles, but it is more often treated as a way to empirically scale the model. For the STM, the beaming parameter can vary from asteroid to asteroid but is assumed constant over wavelength, and the value of 0.756 was determined empirically by Lebofsky et al. (1986) from thermal IR measurements of (1) Ceres and (2) Pallas. For the FRM, the beaming parameter is fixed at π. For the NEATM, the beaming parameter is a free parameter that varies to fit the data. The STM with 0 solar phase angle is the equivalent of a nonrotating spherical blackbody and predicts the maximum possible flux density for given observation geometry and physical parameters, while the FRM is considered the minimum possible. The NEATM has become the standard model for thermal asteroid analysis following its wide use by the NEOWISE Collaboration (Mainzer et al. 2011).

To identify asteroids present in those fields, we compiled a list of potentially visible objects. First, we queried the JPL Small-body Database (SBD) Search Engine (Giorgini 2020) to generate a list of all small bodies with reported values of effective spherical diameter D, perihelion distance q, and minimum orbit intersection distance (MOID). Next, we estimated the maximum possible flux density of each of those objects with the STM. We considered maximum possible flux by assuming values of 1 for emissivity and 0 for albedo, and using q as solar distance and MOID as Earth distance for optimal viewing geometry. We adopted the standard empirical assumption of 0.756 for the model's beaming parameter. Finally, we eliminated all asteroids for which the maximum possible flux fell below 0.5 mJy, which would correspond to roughly a 2σ fluctuation at the projected depth of the main SPT-3G field after 5 yr of observing. However, we maintained all comets and near-Earth objects as potentially interesting objects regardless of the maximum possible flux. This resulted in a list of 5885 objects of interest.

After compiling a list of viable observation candidates, we identified those that were within our observation fields during our observation periods. We did so using `astroquery`, a set of Python tools developed by Ginsburg et al. (2019) to request data from online astronomical databases and web services. First, we queried JPL HORIZONS Web-Interface (Giorgini et al. 1996) to generate ephemerides for each asteroid on each day we observe in each field. Next, we filtered the list of objects by removing all those that were outside of the fields during the entire observation periods. Then, we queried the JPL SBD for each object's diameter and albedo, and we used these values and their ephemerides in the STM to estimate the objects' fluxes. Finally, we estimated the expected noise levels by scaling the fully integrated noise levels reported in Bleem et al. (2020) depending on the number of observations in which each asteroid was present. We computed a prediction of S/N by dividing each asteroid's average flux density by its estimated noise level. Although we attempted to detect all 136 objects that passed through our fields, we only present results here for those three asteroids with a predicted S/N at 2.0 mm greater than 5.

We note that these predicted S/N values are likely upper limits due to multiple assumptions that affect the asteroids' temperatures. For one, the STM models asteroid *surface* temperatures, and we expect that millimeter emission originates from cooler, subsurface regions (Keihm et al. 2013). Likewise, the STM models the limit of a nonrotating asteroid, in which case the asteroid reaches the maximum possible temperature, so we expect that a realistic, rotating asteroid would be cooler. Predicted S/N values will also differ from measured values depending on the asteroids' rotations relative to the observer. That is, an asteroid whose hot subsolar point is rotating away from the observer is in thermal *morning* and will appear less bright than an asteroid whose hot subsolar point is rotating toward the observer in thermal *afternoon*.

4. Methods for Detecting Asteroids and Constraining Their Properties

Using the methods in Section 3, we compile a list of asteroids that are known to pass through our fields during our observation periods. In this section, we describe the methods we used to measure emission from the selected asteroids in SPT data.

First, we calculate the noise in each individual observation map, which were previously constructed from ∼2.5 hr long observations of each field. We also compare the apparent positions of bright extragalactic sources in each individual observation map with the known positions of those sources in the AT20G catalog to double-check astrometry (Murphy et al. 2010). We then *co-add* the individual observation maps of each field, excluding any observations that were outliers in the distribution of map noise or astrometry. For details on the co-adding process, we refer readers to Bleem et al. (2020) and Everett et al. (2020). A co-added map measures the sky's average signal; each pixel's value in the co-added map is the average of that pixel from the input maps weighted by inverse variance. Because the co-added maps are averages, we retain power dominated by static sources, but we average out power from variable sources and moving sources, including asteroids in particular. Next, we subtract the co-added map from each individual observation map to create *differenced maps*. Because we subtracted off the power from static sources, these differenced maps should contain only noise and flux from transient and variable sources. When subtracting the co-added map, which includes transient and variable sources, we do introduce a bias by removing some of the sources' power, but this bias is at the percent level since no asteroid observation contributes more than ∼1.5% to the co-added map. This bias would be much larger for asteroids moving at angular speeds much slower than the size of one SPTpol beam between observations, or roughly $29'' \, \mathrm{hr}^{-1}$. In this work we analyze asteroids moving quickly enough that this bias is not concerning, with (324) Bamberga moving the slowest at an average angular speed of $\sim 20'' \, \mathrm{hr}^{-1}$. Because our goal is to detect asteroids, the differenced maps are the primary form of data that we analyze in this work.

To enhance the sensitivity of the asteroid search, we choose to look at the locations of known asteroids, which requires precisely knowing those locations. Some asteroids can move across the sky at angular speeds such that the change in their position over an hour is comparable to the SPT beam size. Since each observation lasts roughly 2 hr, we must more precisely define what time we scan over any asteroid. We maintain some precision by considering the SPT's scanning strategy, which involves scanning back and forth in azimuth before stepping in elevation, which at the South Pole is equivalent to stepping in decl. If we know an asteroid's decl. around the time of observation, we can interpolate a more precise time at which we scan over the asteroid. First, we queried JPL HORIZONS Web-Interface using `astroquery` to generate ephemerides for all asteroids at the time halfway through each observation, an initial guess. Then, we estimated the time at which the telescope would scan over the asteroid and re-queried JPL HORIZONS Web-Interface to obtain a more precise location. Given typical MBA motions, we assume our positional errors to be much less than the SPT beam size.

Using these more precise asteroid locations, we cut out small regions of each differenced map centered on the asteroid location. We conduct multiple analyses on these cutouts. To report mean flux measurements, we co-add the cutouts and filter the co-added cutout with a *matched filter* that maximizes the S/N for point sources. For details on matched filtering SPT data, we refer the reader to Everett et al. (2020). The resulting measurements are in units of T_{CMB}; i.e., map values are expressed as equivalent fluctuations from the mean CMB blackbody temperature of 2.726 K. We convert the value of the center pixel to report flux density in units of millijansky. We calculate uncertainties and S/N by computing the rms noise in areas of the co-added cutout between $1.'5$ and $15'$ away from the asteroid. We report our mean flux measurements in Section 5.

We can calculate other useful information from mean flux measurements. To do so, we use the NEATM to remain consistent with standard reporting of thermal emission measurements. NEOWISE reported diameters, albedos, and beaming parameters for thousands of asteroids, and we use those values to predict our asteroids' expected fluxes more reliably (Mainzer et al. 2019). Once we compute the NEATM flux predictions, we can calculate effective emissivities in each band by dividing the measured flux by the model flux. Likewise, we can use the NEATM to solve for the subsolar temperature, which would produce the fluxes we measure, and we scale these temperatures by solar distance $r_\odot$ according to the NEATM's assumed dependence of $r_\odot^{-1/2}$. Not only can this

brightness temperature be viewed as another way to report mean flux density, but calculated brightness temperature and effective emissivity can also be viewed as probes of the long-wavelength emission drop described in Section 1. Furthermore, because we make flux measurements at multiple wavelengths, we can calculate the spectral index α between the two wavelengths. We define α in terms of measured flux S_ν at frequency ν such that

$$S_\nu \sim \nu^\alpha, \qquad (1)$$

so that it is easy to compare to expected thermal emission with $\alpha = 2$. We report our predicted fluxes, calculated effective emissivities, calculated brightness temperatures, and calculated spectral indices in Section 5.

SPTpol does not have high enough sensitivity to detect most asteroids with high significance in individual observations, but we can still consider the flux of the center pixel as a function of time, i.e., the target's light curve. We create the light curves by matched filtering each non-co-added differenced map and plotting flux versus time of observation. In this paper, we create the light curves only for 2.0 mm data because our observations at this wavelength have higher S/N and do not require additional elevation-dependence calibration like our 3.2 mm data. Light curves are important because observed flux density changes depending on viewing geometry. We test whether we detect the expected change in flux density by calculating the difference in χ^2 between models that consider only constant flux from the source versus constant flux plus variation as predicted by the NEATM.

Asteroids in general are not spherical, so as they rotate while traveling through space, we expect to observe a periodic modulation in their light curves. If we can detect modulation of this type in the light curves, we can infer information about an asteroid's shape, rotational period, and other properties. First, we scale the light curves by a correction factor to account for flux changes due to viewing geometry. This is done by calculating the mean flux predicted by the NEATM and scaling the light curve to that value. For a sense of what that scaling might look like, consider the STM in the long-wavelength Rayleigh–Jeans limit, in which case flux density F varies like

$$F \sim r_\odot^{-1/2} r_\oplus^{-2} 10^{-0.004\alpha}, \qquad (2)$$

where $r_\odot$ is the solar distance to the asteroid, $r_\oplus$ is Earth's distance to the asteroid, and α is the solar phase angle measured in degrees, an empirical fit. We compute scaling factors to mean values of $r_\odot$, $r_\oplus$, and α based on NEATM predictions, which is comparable at the percent level to using the above functional form. Next, we compute Lomb–Scargle periodograms to try to detect statistically significant periods. For details on the periodogram, we refer readers to VanderPlas (2018). Finally, if the asteroid has a known period, we can also *fold* the light curve by plotting flux versus observation time modulo rotation period. When we fold the light curve in this way, we plot flux as a function of the rotational phase, and we fit a sinusoidal function to place limits on modulation amplitudes at millimeter wavelengths. To first order, asteroids are ellipsoids, so we would expect the most observable modulation to be sinusoidal with a period half that of the asteroid's known rotational period.

One caveat to our light-curve analysis is that each asteroid is scanned over multiple times in each ~2.5 hr individual observation. This introduces two effects: an inexactness for the time observed and an averaging of flux from the asteroid during that time. If the rotation period of the observed asteroid is short compared to the timescale over which the asteroid is observed, these effects will both reduce sensitivity to the brightness modulation induced by rotation. For the SPTpol observations under study, in which the telescope is scanned back and forth in azimuth and then stepped in elevation, the relevant observation timescale is the time during which a particular sky elevation is within the field of view of the camera. The elevation extent of the SPTpol camera is roughly 1°; thus, in a ~2.5 hr observation of a 10° field, a particular elevation will be visible for approximately 15 minutes. This is much less than the multiple-hour rotational periods of our asteroids of interest, and we conclude that our sensitivity to rotational effects is not compromised by these effects.[53]

5. Results

Using the methods described in Section 3, we compile a list of 54 objects in RA13HDEC-25 and 82 objects in RA13HDEC-25 that are within the fields during at least one observation, and we predict the integrated S/N for each asteroid. This information—mean model flux, number of observations present, and corresponding predicted S/N at 2.0 mm—is summarized in Figure 2. We present these predictions only at 2.0 mm because we expect a larger emitted flux at shorter wavelengths and a better point-source sensitivity in that band. As can be seen in Figure 2, only three asteroids are present for long enough and with great enough mean flux to be detected at S/N > 5. We predict that the only asteroid with S/N > 5 in RA13HDEC-25 is (324) Bamberga with S/N ~ 12.5 and that the only asteroids with S/N > 5 in RA23HDEC-25 are (13) Egeria and (22) Kalliope with S/N ~13.5 and ~10.7, respectively. We performed the differencing and co-adding procedures described in Section 4 on all 136 selected objects in our fields, and we were indeed able to detect only those three asteroids with high significance. The rest of this section will focus on those three asteroids.

(324) Bamberga is a large MBA with an effective body diameter of 220.7 km (Masiero et al. 2014). We observe (324) Bamberga in RA13HDEC-25 during 115 observations between 2016 February 13 and 2016 March 22 with a mean observing geometry of 3.58 au solar distance, 2.78 au Earth distance, and 10°.2 solar phase angle. Its trajectory during this time is plotted in Figure 3, and details of observation geometries are included in Appendix A. Using the methods described in Section 4, we co-add observations made during this time, and we show cutouts of the resulting maps in Figure 4. From these maps, we detect the asteroid with S/N = 4.1 and 11.2 and record an average flux of 16.0 ± 3.9 and 30.6 ± 2.7 mJy, at 3.2 and 2.0 mm, respectively, corresponding to a spectral index of 1.5 ± 0.6. The measured average flux levels are roughly consistent with those predicted by the NEATM, as shown in Table 1. We calculate the expected mean flux density, effective emissivity, and brightness temperature in Table 1 using 0.89 for the NEATM beaming parameter, as reported by NEOWISE (Mainzer et al. 2019). Its light curve is plotted along with flux predicted by the NEATM in Figure 5. We detect variation in the light curve of the form predicted by the NEATM with a χ^2

---

[53] We note that we could restore nearly full sensitivity to changing asteroid brightness by analyzing single telescope scans individually, as was done in Guns et al. (2021), but the scaling arguments above imply this would not improve our sensitivity to asteroid brightness changes in any material way.
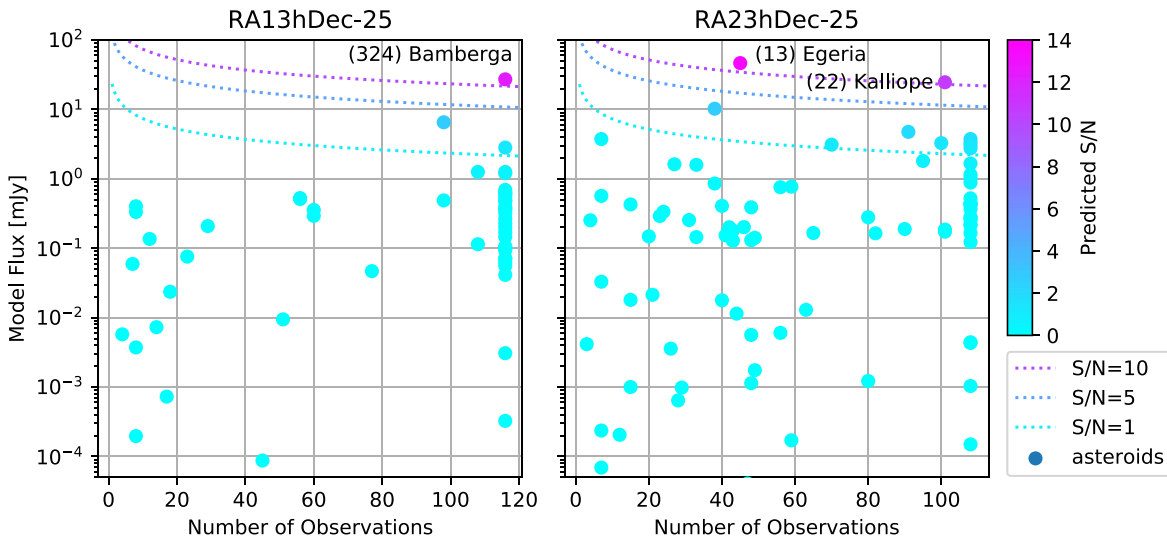
Figure 2. Predicted asteroid S/N at 2.0 mm in the RA13HDEC-25 and RA23HDEC-25 fields. We base these predictions on the number of observations in which the asteroid is present in the field as well as the mean asteroid flux modeled by STM at 2.0 mm during those observations. Each point in the plot represents an asteroid present in the field during at least one observation. The dotted lines trace out levels of constant S/N at values equal to 1, 5, and 10.
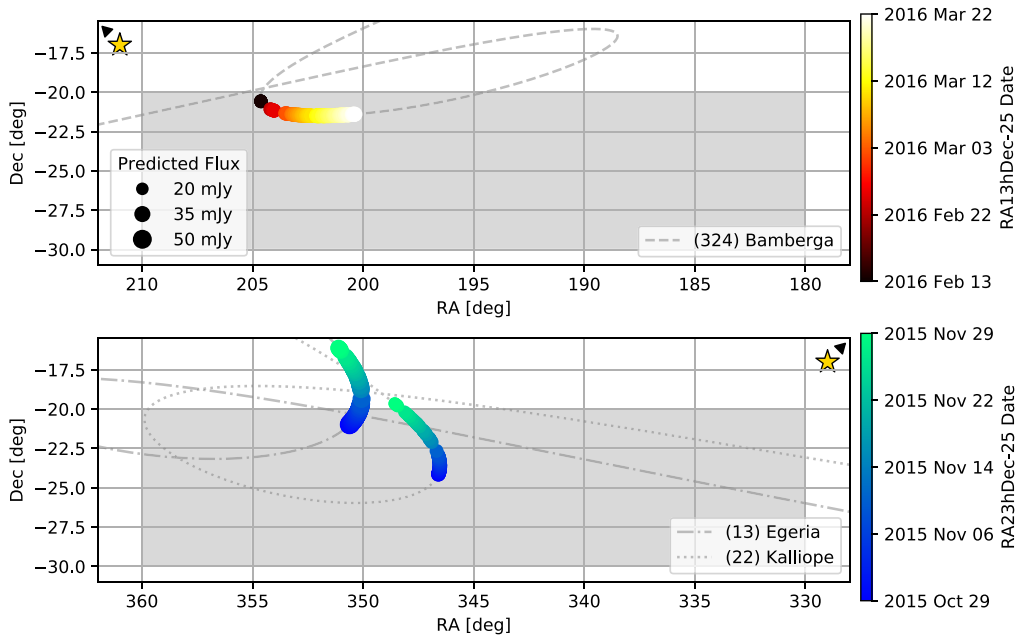

Figure 3. Trajectories of (324) Bamberga through RA13HDEC-25 (top panel) and (13) Egeria and (22) Kalliope through RA23HDEC-25 (bottom panel). The shaded gray regions represent the field boundaries. The dotted and dashed lines represent the asteroids' long-term trajectories, which trace out loops due to parallax motion. Each colored dot represents the asteroids' positions at the time of an observation of the field. The size of each dot represents flux density at 2.0 mm predicted by the NEATM. The stars and arrows point toward the mean locations of the Sun during the observation periods.

difference of 5.08 compared to a constant flux model, corresponding to a p-value of 0.0014.

(13) Egeria is a large MBA with an effective body diameter of 202.6 km (Nugent et al. 2015). We observe (13) Egeria in RA23HDEC-25 during 45 observations from 2015 October 29 until it exits the field on 2015 November 5 with a mean observing geometry of 2.68 au solar distance, 2.02 au Earth distance, and 18°.2 solar phase angle. Its trajectory during this time is plotted in Figure 3, and details of observation geometries are included in Appendix A. We show cutouts of the averaged observation maps in Figure 4. From these maps, we detect the asteroid with S/N = 1.7 and 10.4 and record an average flux of 11.6 ± 6.9 and 44.5 ± 4.3 mJy, at 3.2 and 2.0 mm, respectively, corresponding to a spectral index of 3.1 ± 1.4. Note that unlike (324) Bamberga

and (22) Kalliope, NEOWISE was unable to fit a value for the NEATM beaming parameter for (13) Egeria, so we use their assumed value of 0.95 to calculate expected mean flux density, effective emissivity, and brightness temperature in Table 1 (Mainzer et al. 2019). The measured average flux level at 2.0 mm is roughly consistent with that predicted by the NEATM, as shown in Table 1. Its light curve is plotted along with flux predicted by the NEATM in Figure 5. Egeria's light curve shows a mild preference for flux change opposite to the NEATM prediction, but this measurement is not statistically significant.

(22) Kalliope is a large MBA with an effective body diameter of 167.5 km (Masiero et al. 2014). We observe (22) Kalliope in RA23HDEC-25 during 100 observations from 2015 October 29 until it exits the field on 2015 November 26 with a
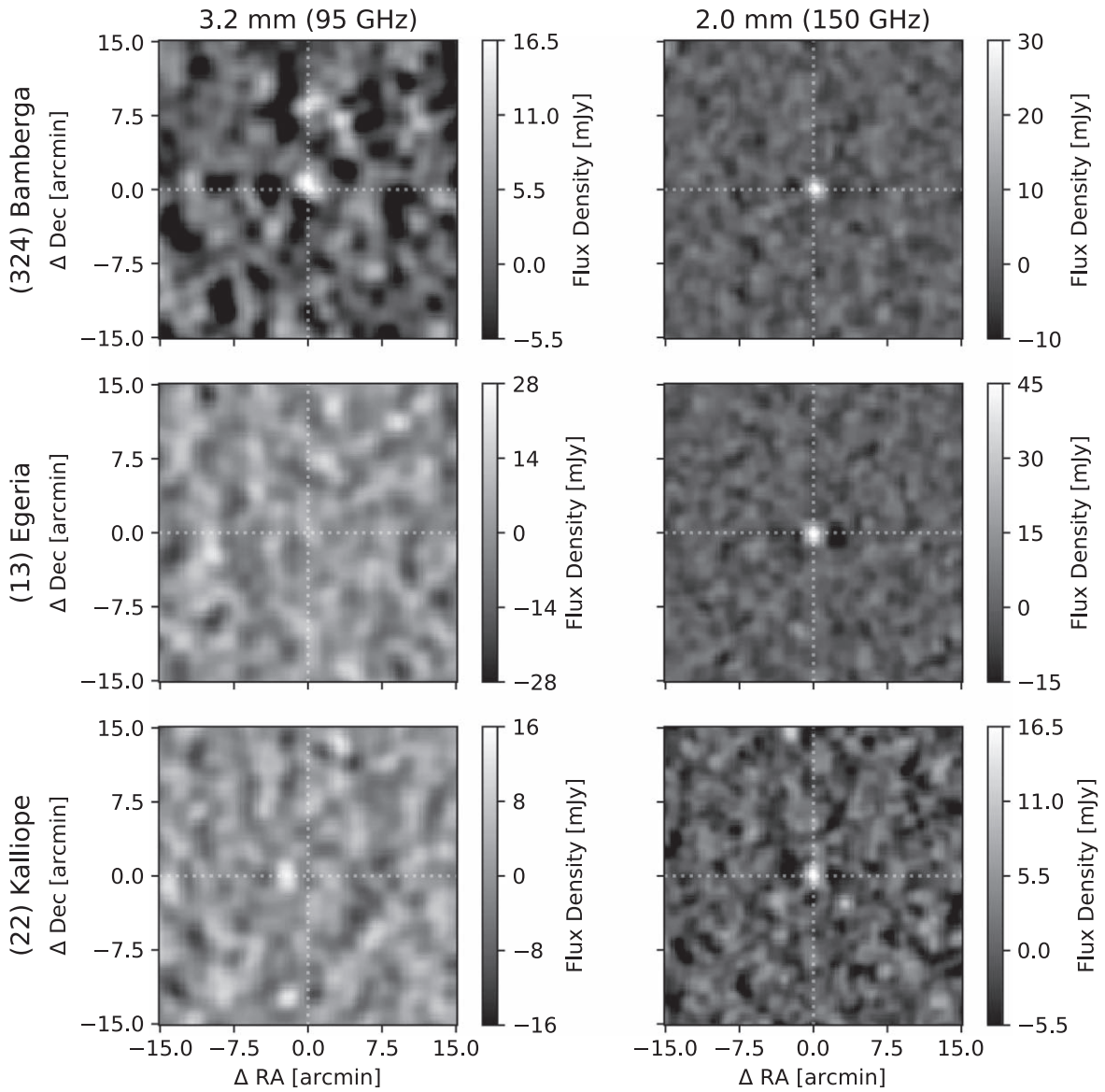
Figure 4. Mean flux measurements of (324) Bamberga (top horizontal panels), (13) Egeria (middle horizontal panels), and (22) Kalliope (bottom horizontal panels) at 3.2 mm (left vertical panels) and 2.0 mm (right vertical panels). Color scales for (13) Egeria and (22) Kalliope at 3.2 mm are set at 4σ levels; the rest peak near the mean flux values detected for each asteroid.

Table 1
Asteroid Detections and Constrained Properties

	(324) Bamberga		(13) Egeria		(22) Kalliope	
	3.2 mm	2.0 mm	3.2 mm	2.0 mm	3.2 mm	2.0 mm
Measured S/N	4.1	11.2	1.7	10.4	−0.8	6.1
Measured mean flux (mJy)	16.0 ± 3.9	30.6 ± 2.7	11.6 ± 6.9	44.5 ± 4.3	-3.1 ± 4.0	16.5 ± 2.7
Predicted mean flux (mJy)	11.8	28.1	20.7	49.6	10.7	25.6
Predicted flux range (mJy)	9.3–11.9	22.2–28.5	17.1–21.4	40.8–51.4	9.2–11.2	21.9–26.7
Effective emissivity	1.36 ± 0.33	1.09 ± 0.10	<1.23	0.90 ± 0.09	<0.46	0.64 ± 0.11
Brightness temperature (K AU$^{1/2}$)	546.9 ± 132.9	438.4 ± 38.4	<488.1	356.7 ± 33.5	<176.9	246.6 ± 39.6
Max. modulation amplitude	$\cdots$	$<33.6\%$	$\cdots$	$<43.3\%$	$\cdots$	$<73.2\%$
Spectral index	1.5 ± 0.6		3.1 ± 1.4		>1.8	

Note. Measurements of flux density and S/N, predictions of flux density, and measurements of or limits on effective emissivity, brightness temperature as a function of solar distance, and light-curve modulation amplitude for the three asteroids in RA13HDEC-25 and RA23HDEC-25 with S/N > 5. We calculate the predicted mean flux using the NEATM, while we calculate the lower and upper values of the predicted flux range with the FRM and STM, respectively. We report $\pm$ values with 1σ significance and upper limits with 2σ significance. Uncertainties reported in this table are pure statistical uncertainties and should be added in quadrature with subdominant systematic uncertainties. The lower limit on the spectral index for (22) Kalliope is estimated using upper and lower 2σ flux measurements at 3.2 and 2.0 mm, respectively.
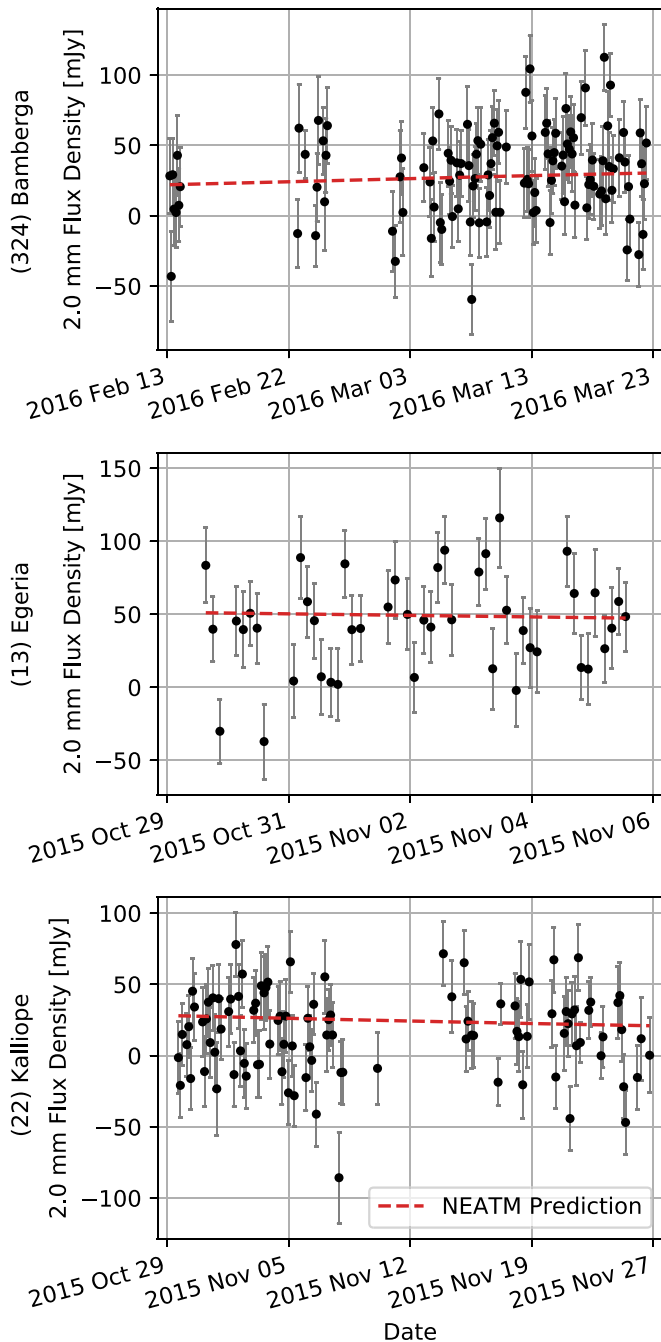
Figure 5. Light curves of (324) Bamberga (top panel), (13) Egeria (middle panel), and (22) Kalliope (bottom panel) at 2.0 mm. The dashed red lines represent NEATM predictions for flux density. (324) Bamberga is the only asteroid for which we detect statistically significant variation in the light curve of the form predicted by the NEATM.

mean observing geometry of 2.76 au solar distance, 2.25 au Earth distance, and 19°5 solar phase angle. Its trajectory during this time is plotted in Figure 3, and details of observation geometries are included in Appendix A. We show cutouts of the averaged observation maps in Figure 4. From these maps, we detect the asteroid with S/N = 6.1 at 2.0 mm and record an average flux of -3.1 ± 4.0 and 16.5 ± 2.7 mJy, at 3.2 and 2.0 mm, respectively, corresponding to an estimated lower limit on the spectral index of 1.8 at 2σ significance. We calculate the expected mean flux density, effective emissivity, and brightness temperature in Table 1 using 1.081 for the NEATM

beaming parameter, as reported by NEOWISE (Mainzer et al. 2019). The measured average flux level at 2.0 mm is consistent with that predicted by the NEATM and an effective emissivity of 0.64 ± 0.11, as shown in Table 1. (22) Kalliope has the lowest effective emissivity of the three asteroids, and the calculated upper limit on effective emissivity at 3.2 mm is significantly lower than that calculated at 2.0 mm. Its light curve is plotted along with flux predicted by the NEATM in Figure 5. The light curve does not show evidence of brightness modulation beyond a constant model.

(22) Kalliope is part of a binary system with its satellite Linus. Studies of (22) Kalliope report that Linus is dimmer by a factor of 25 ± 5, so we ignore the contribution of Linus to mean flux (Margot & Brown 2003).

When we compare the light curves plotted in Figure 5 with NEATM predictions, we calculate excess variance beyond the model. This excess variance in asteroid light curves suggests that we may be missing something in either our flux calculations or our model, but we are confident that this is not due to day-to-day calibration given our checks described in Section 2.3.2. We perform a check by creating light curves of null off-target pixels from differenced maps, and we confirm that these light curves are statistically consistent with zero.

Because we detect the mean flux from these three asteroids with a high S/N at 2.0 mm, we also study their light curves at this wavelength in an attempt to detect the effect of rotation. We calculate a Lomb–Scargle periodogram for each light curve, and we do not detect significant periodicity in any of the three. We then adopt external constraints on the rotational period of the asteroids and attempt to detect the modulation effect in folded light curves. We assume rotational periods based on published observations at other wavelengths reported by the Minor Planet Center's Asteroid Lightcurve Database (LCDB) (Warner et al. 2009). We assume that (324) Bamberga rotates with a rotational period of 29.43 hr, (13) Egeria with a rotational period of 7.045 hr, and (22) Kalliope with a rotational period of 4.1483 hr. We fold the light curve on the rotational periods and show the resulting phased light curves in Figure 6. None of these light curves modulate enough at 2.0 mm to detect within our sensitivity, and we use that fact to set limits on maximum possible modulation amplitude, which we list in Table 1.

6. Discussion

We measured mean flux densities for (324) Bamberga and (13) Egeria that were relatively close to NEATM predictions. Meanwhile, we measured mean flux densities for (22) Kalliope well below the predicted values.

This discrepancy may be explained by considering the asteroids' compositions and physical properties. For instance, radar albedo measurements can inform knowledge of near-surface density and porosity. In general, lower radar albedo is correlated with lower density or higher porosity, and asteroids of similar classification have similar radar albedo. (22) Kalliope, an M-type asteroid, has a radar albedo around 0.18 ± 0.05 (Shepard et al. 2015), consistent with an average 0.294 ± 0.135 for other M types (Virkki et al. 2014). Given (22) Kalliope's relatively high bulk density of about 3.4 g cm^{-3} (Descamps et al. 2008), this suggests it has a porous surface composed of a mixture of silicates and iron. (324) Bamberga, a C-type asteroid, and (13) Egeria, a G-type asteroid, have much lower radar albedos of 0.031 ± 0.009 and 0.059 ± 0.023, respectively (Magri et al. 2007). This suggests that (324)
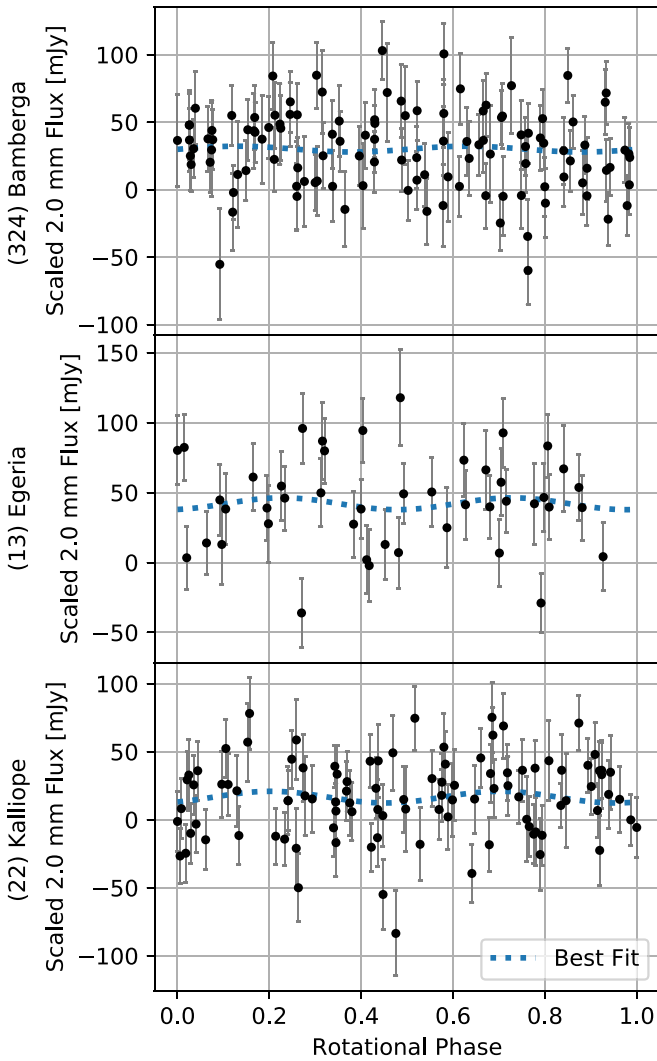
Figure 6. Phased light curves of (324) Bamberga (top panel), (13) Egeria (middle panel), and (22) Kalliope (bottom panel) at 2.0 mm, folded over the rotational period and scaled to mean observed solar distance, Earth distance, and solar phase angle as described in Section 4. The dotted blue lines represent the sinusoidal function that best fits the data, although none of these fits are statistically significant. The sinusoidal periods are constrained to half the rotational periods, but the amplitudes and phases are free parameters.

Bamberga and (13) Egeria have lower near-surface density or higher porosity than (22) Kalliope.

Consider also the thermal inertia, Γ, of an object, defined as

$$\Gamma = \sqrt{\rho C k}, \tag{3}$$

where ρ is the object's density, C is the object's heat capacity, and k is the object's thermal conductivity. Greater thermal inertia corresponds with an object's greater resistance to changing temperature. (22) Kalliope's higher near-surface density than (324) Bamberga and (13) Egeria suggests a higher thermal inertia. Indeed, studies have shown that M-type asteroids like (22) Kalliope in general have much higher values of thermal inertia than other carbonaceous asteroids like (324) Bamberga and (13) Egeria (Opeil et al. 2010). (22) Kalliope's greater thermal inertia may impact its millimeter flux in two particular ways.

One effect of greater thermal inertia is that the resistance to changing temperature causes less diurnal temperature variation: the asteroid's dayside has a lower temperature and therefore

decreased radiated flux, and the asteroid's nightside has a higher temperature and therefore increased radiated flux. Overall, this effect leads to a net decrease in expected flux for most objects viewed at less than a 90° solar phase angle, i.e., those objects with a solar distance greater than 1 au like the vast majority of objects potentially analyzed with SPT data. Flux models like the NEATM and STM assume the case of low thermal inertias, in which one subsolar point reaches maximum temperature equivalent to a nonrotating body. The FRM assumes the case of large thermal inertia, wherein the asteroid's whole equator reaches maximum temperature as the asteroid rotates. We can estimate how well we expect the NEATM to predict flux densities by calculating the *thermal parameter* Θ as defined by Spencer et al. (1989):

$$\Theta = \frac{\Gamma \sqrt{\omega}}{\epsilon \sigma T_{ss}^3}, \tag{4}$$

where ω is angular rotational frequency, ϵ is emissivity, σ is the Stefan–Boltzmann constant, and T_{ss} is subsolar temperature. Small Θ values (~ 0) suggest high diurnal temperature variation akin to STM and NEATM predictions, while large Θ values (roughly $\gtrsim 10$) suggest low diurnal temperature variation akin to FRM predictions.

It is tempting to explain (22) Kalliope's lower flux as caused by low diurnal temperature variation. We can approximate emissivity around 0.9, subsolar temperature around 222 K from the NEATM, and upper limit on the thermal inertia of $250 \, \text{Jm}^{-2} \, \text{K}^{-1} \, \text{s}^{-1/2}$ from Marchis et al. (2012) to find that (22) Kalliope could have $\Theta \sim 9$. This value would be even higher assuming a lower surface temperature or emissivity. We expect that (324) Bamberga and (13) Egeria would have a much lower thermal parameter given that we expect they have lower thermal inertia and that their rotational periods are roughly 7 and 2 times as long as (22) Kalliope's, respectively. This calculation suggests that (22) Kalliope may have much lower diurnal temperature variation than the NEATM might predict. However, this cannot account for the entirety of (22) Kalliope's lower effective emissivity given that our measured mean flux is significantly lower than the bound predicted by the FRM.

Furthermore, it is even clearer that rotational effects cannot solely explain (22) Kalliope's lower effective emissivity when its spin axis orientation is considered. The Database of Asteroid Models from Inversion Techniques (DAMIT)[54] is a database of three-dimensional models for many asteroids, including (22) Kalliope (Sidorin & Kaasalainen, M 2010). (22) Kalliope's proposed shape models suggest a spin axis with an ecliptic latitude of 3° and ecliptic longitude of 196° (Kaasalainen et al. 2002; Ďurech et al. 2011; Hanuš et al. 2017; Vernazza et al. 2021). This low ecliptic latitude means (22) Kalliope has a large axial tilt relative to its orbital axis. Given our viewing geometry, (22) Kalliope's subsolar point and rotational north pole are both near each other and visible to the observer. This geometry suggests that the same areas of (22) Kalliope's surface are being heated consistently.

Another effect of greater thermal inertia is that the resistance to changing temperature means that the subsurface regions from which millimeter emission originates may be cooler, causing a lower measured millimeter flux. Although this is a possible explanation for the observed flux from (22) Kalliope,

---

[54] https://astro.troja.mff.cuni.cz/projects/damit/

it is also unlikely given that the same areas of (22) Kalliope's surface are being heated consistently.

Alternatively, scattering by surface particles may explain (22) Kalliope's lower measured millimeter flux. For instance, (16) Psyche is another M-type asteroid that has a comparable surface and was analyzed in detail at around 1.3 mm by de Kleer et al. (2021). They found (16) Psyche had a millimeter emissivity of 0.61 ± 0.02, which they attributed to a highly scattering surface, and they ruled out the possibility that this measurement was caused by cooler subsurface emission. To definitively draw similar conclusions for (22) Kalliope, we would need to conduct more advanced thermophysical modeling beyond the scope of this analysis, which attempted primarily to test our ability to make these mm flux measurements. Nevertheless, it is reassuring that our measurements of (22) Kalliope are comparable to modern measurements at millimeter wavelengths of other asteroids with comparable surface composition.

To interpret our limits on rotational light-curve amplitude in context, we consider previous measurements of these asteroids' light curves and shapes. Shape models for all three asteroids were recently created by Vernazza et al. (2021) including measures of their elliptical-model-based eccentricities c/a, and maximum light-curve modulation is reported on the LCDB. (324) Bamberga is fairly round with a reported c/a of 0.96 ± 0.05, so we should expect a small value for modulation amplitude. Indeed, the maximum flux modulation amplitude reported on the LCDB is 12%. (13) Egeria is notably more irregular in shape and has a reported c/a of 0.76 ± 0.06. Maximum flux modulation amplitude reported on the LCDB is as great as 54%, though some reports are lower than that. Many of these observations also show a notably asymmetric light curve, which hurts our assumption that expected folded light-curve modulation will be purely sinusoidal. Nevertheless, a pure sinusoid should still match the modulation to first order. (22) Kalliope is the most elliptical of the three asteroids with a reported c/a of 0.59 ± 0.02, so depending on viewing geometry we could expect the largest value for modulation amplitude from this object. Maximum flux modulation amplitudes reported on the LCDB are as great as 63%, though these also vary. However, given the orientation of (22) Kalliope's spin axis as explained before, we should expect to measure a very small modulation amplitude. Even without considering spin axis orientation for any of our three measured asteroids, our limits on modulation amplitude are less restrictive than those previously determined by others.

7. Predicted Asteroid Detections for Other SPT Surveys

As described in Section 2.1, the SPT has been equipped with three separate cameras over its lifetime: SPT-SZ, SPTpol, and SPT-3G. With SPT-SZ, observations were made of a patch-work of many fields to comprise its survey. With SPTpol and SPT-3G, observations were made of main, deep fields during austral winters and various other fields for shorter durations during austral summers. We refer to all observations made to date collectively as the SPT's historic data, while we refer to future observations planned with the SPT-3G camera as the SPT's future data. Using the methods described in Section 3, we compile lists of all asteroids present in historic and future data and predict their S/N. We show all objects we expect to observe in Figure 7 and summarize these predictions in Table 2. We provide detailed field boundaries, observation periods, and object lists in Appendix B.

We note that the SPT-3G camera has higher instantaneous sensitivity than the SPT-SZ and SPTpol cameras, so we expect to measure more asteroids and at improved sensitivities in SPT-3G data. We expect that the improved sensitivity will allow us to place tighter constraints on both mean flux measurements and modulation amplitudes of folded light curves. For a rough estimation, our ability to constrain modulation amplitudes will depend on the S/N available in roughly one-fourth of an object's rotation period, which is roughly one-half of the S/N shown in Figure 7.

7.1. Validation of Prediction Model with SPT-3G 1500d Data

As shown in Appendix B, we should see two asteroids at high S/N in the SPT-3G main survey field during the 2020 austral winter. Since maps were generated following each observation of the SPT-3G survey field as part of an online data-quality monitoring pipeline, it was straightforward to extract thumbnail maps around the locations of the asteroids using methods similar to those in Section 4. We constructed a proof-of-concept pipeline for SPT-3G, and although the pipeline was separate, it was similar in construction and methodology to the pipeline used for the detections in SPTpol data.

We report the mean fluxes and S/Ns for the two asteroids with predicted S/N > 5 at 2.0 mm in the 1500 deg^2 survey region during the austral winter 2020. We observe (1093) Freda in 297 observations and measure a mean flux density of 6.3 ± 0.6, 18.7 ± 0.8, and 43.0 ± 3.3 mJy at 3.2, 2.0, and 1.4 mm respectively, corresponding to an S/N of 10.6, 22.9, and 13.1. We observe (772) Tanete in 156 observations and measure a mean flux density of 4.4 ± 0.7, 10.7 ± 1.9, and 27.1 ± 6.0 mJy at 3.2, 2.0, and 1.4 mm respectively, corresponding to an S/N of 6.5, 5.6, and 4.5. We show co-added observation maps of these asteroids in Figure 8.

8. Conclusion

In this work, we have demonstrated that we are able to detect asteroids in millimeter observations of the sky made with the SPT, and we show that we will detect even more asteroids in other historic and future data from the SPT. Using maps from repeated observations of the same area of the sky over the course of months, we measure three asteroids, (324) Bamberga, (13) Egeria, and (22) Kalliope, at wavelengths of 3.2 and 2.0 mm with the SPTpol camera, and we report measurements of the asteroids' mean fluxes at 2.0 mm with an S/N of 11.2, 10.5, and 6.1, respectively. We also report measurements of (324) Bamberga at 3.2 mm with an S/N of 4.1. Although others have studied asteroid thermal emission at mm wavelengths, this work is the first focused analysis of asteroid flux using data taken with the primary science goal of characterizing the CMB.

Observing asteroids with CMB survey data expands the breadth of two separate fields of astronomy. CMB survey scientists can now include asteroid science as part of their data analysis, and they have more scientific use for their historic data. They may perform more focused studies of asteroids in the future, potentially including near-Earth asteroids that pass through survey fields. Meanwhile, asteroid scientists now have access to more data on the thermal emission of asteroids. They can make use of measurements in mm wavelengths made using CMB experiments, especially as the instantaneous sensitivity of CMB cameras improves and allows more precise time-domain astronomy.
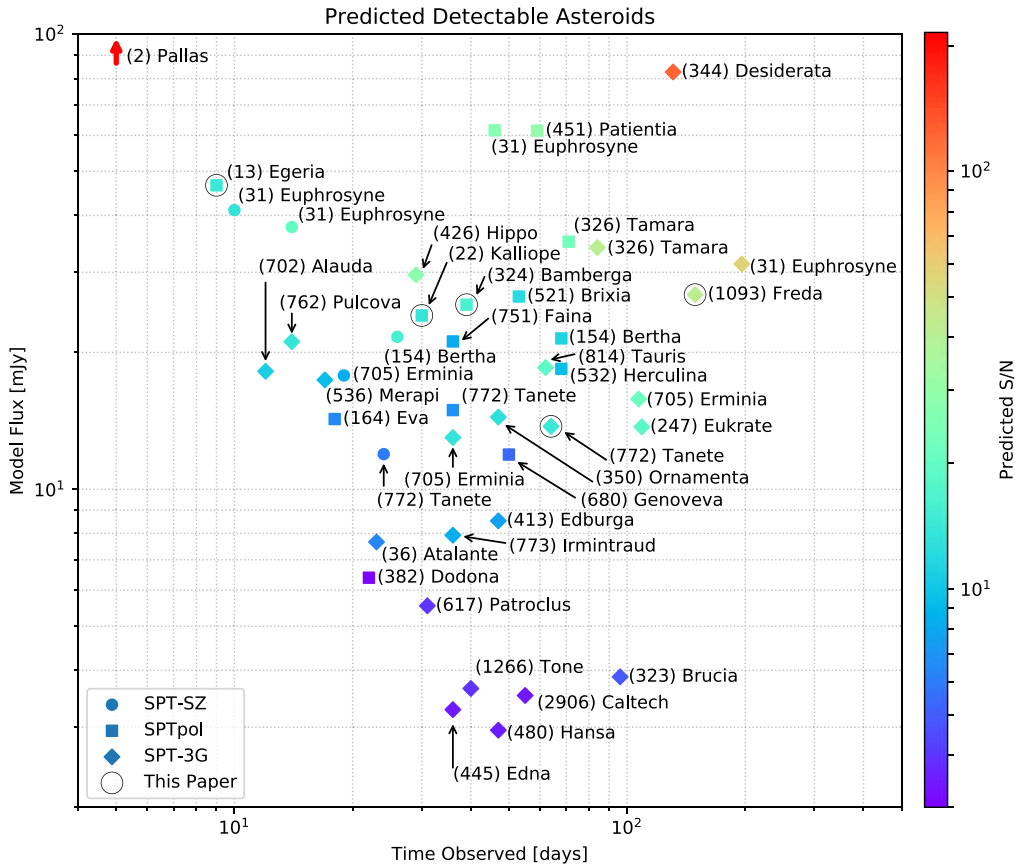
Figure 7. Objects with predicted S/N > 3 at 2.0 mm in all historic and planned future SPT data. We expect to observe (2) Pallas, plotted off scale, with a mean flux density near 650 mJy.

Table 2
Summary of Predicted Detections

Survey	Objects with Predicted S/N > 3
SPT-SZ	4
SPTpol deep ("500d") field	2
SPTpol Summer Fields	12
SPT-3G deep ("1500d") field	14
SPT-3G summer fields	10

Note. Summary of the estimated number of detectable asteroids at 2.0 mm in completed historical and planned future surveys using the SPT. The SPTpol and SPT-3G *deep fields* are those main fields observed during austral winters, while the *summer fields* are those other fields observed during austral summers. Details are included in Appendix B.

Our measurements in millimeter wavelengths come at an important time for asteroid scientists, when studies like Keihm et al. (2013) suggest a paradigm shift in the understanding of asteroid regolith temperatures. We measured the flux from (324) Bamberga to moderate significance at 3.2 mm and high significance at 2.0 mm and found flux densities consistent with model predictions. We measured the flux from (13) Egeria to high significance at 2.0 mm, and we used the lack of a detection at 3.2 mm to place limits on its brightness temperature and effective emissivity at this wavelength. We measured the flux from (22) Kalliope to moderate significance at 2.0 mm and showed a significant decrease in millimeter flux at 3.2 mm compared to 2.0 mm, consistent with previous studies of other large MBAs suggesting a decrease in flux at longer wavelengths. Our

measurements will help place limits on the thermal properties and composition of these asteroids' regoliths.

With historic and future data, we expect to observe 34 total asteroids, including very precise measurements of (2) Pallas and (344) Desiderata; multiple measurements of (31) Euphrosyne, (154) Bertha, (326) Tamara, (705) Erminia, and (772) Tanete; and measurements of (617) Patroclus, a target of NASA's Lucy mission (Levison et al. 2021).

Using data from SPTpol, we made significant measurements of (13) Egeria and (22) Kalliope at only one wavelength, and we did not have high enough sensitivity in individual observations to describe light curves to high accuracy. However, SPT-3G will improve on both of these limitations with its higher sensitivity and third wavelength band, as shown by the detections of (772) Tanete and (1093) Freda. SPT-3G's higher sensitivity will also allow us to observe fainter objects than with SPTpol. In fact, SPT-3G and other future CMB surveys may have to mask asteroids during transient source analysis, since as of the writing of this paper, objects like (344) Desiderata are bright enough to trigger the SPT-3G transient alert system. Furthermore, many of the asteroids detectable with SPT-3G will be observed for longer periods of time than those with SPT-SZ or SPTpol. The longer observation times and higher instantaneous sensitivity of SPT-3G will allow us to place tighter constraints on modulation amplitude for those asteroids, and potentially to detect modulations of more than a few percent. With SPT-3G sensitivity, we will be able to observe more asteroids at more wavelengths, and, for many of them, over longer times.

By repurposing historic and future data from the SPT, we will observe asteroids without needing to dedicate telescope observation time to do so. The measurements we make will
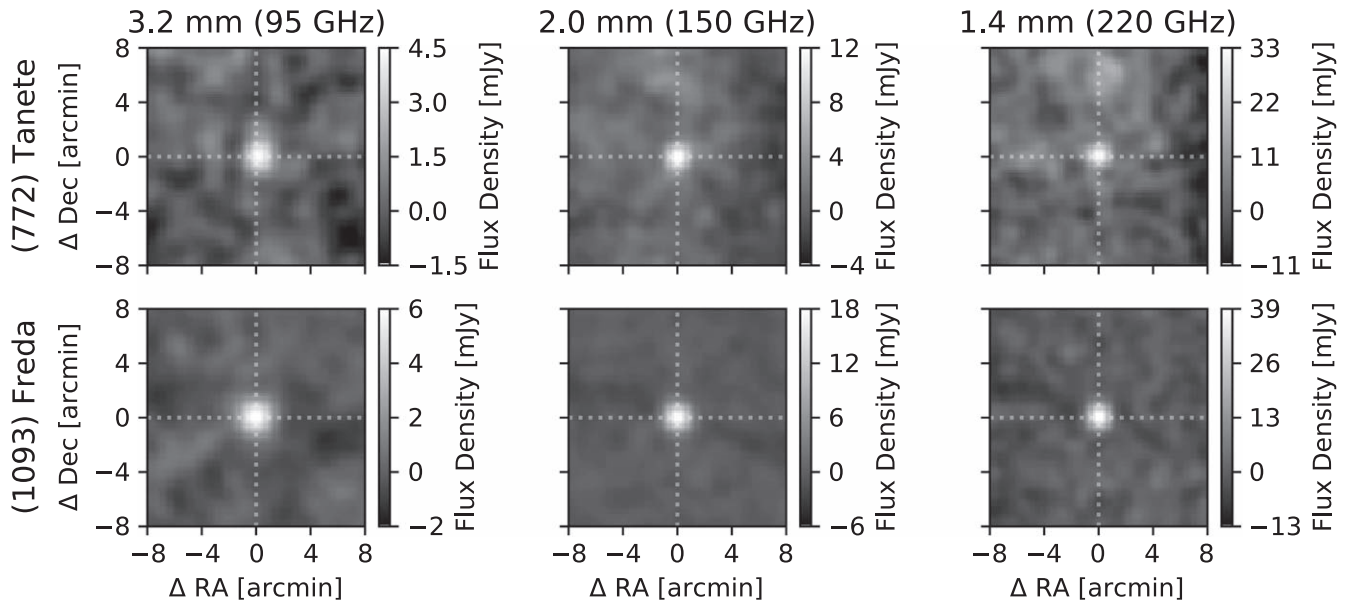
Figure 8. Mean flux measurements of (772) Tanete (top horizontal panels) and (1093) Freda (bottom horizontal panels) at 3.2 mm (left vertical panels), 2.0 mm (middle vertical panels), and 1.4 mm (right vertical panels). These measurements were taken with the SPT-3G camera in the main survey field during the 2020 austral winter.

provide new constraints on the thermal properties and compositions of asteroid regoliths.

Appendix A
Observation Geometries

This section describes details of the observation geometries for the three asteroids analyzed in Section 5. Figure 9 shows the asteroids' solar distance, earth distance, and solar phase angle during observations. This information was queried from JPL HORIZONS.
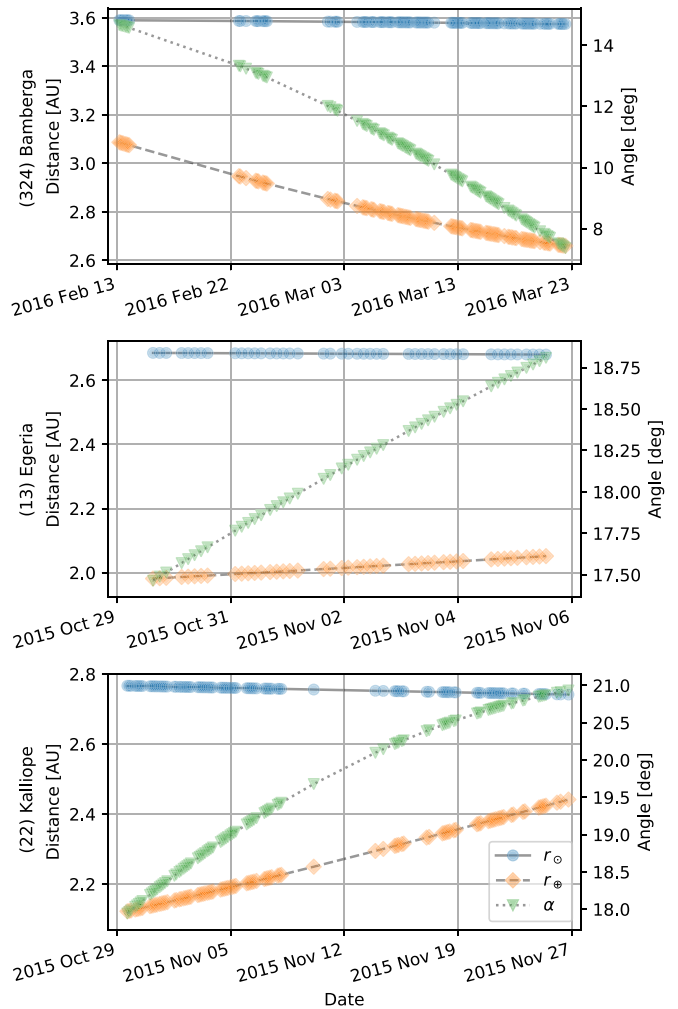
Figure 9. Observation geometries for (324) Bamberga (top panel), (13) Egeria (middle panel), and (22) Kalliope (bottom panel). Each point represents one observation. Solar distance $r_\odot$ and Earth distance $r_\oplus$ are plotted in astronomical units, and solar phase angle α is plotted in degrees.

Appendix B
Asteroids in Historic Data

This section contains a detailed definition of each observation field's boundaries, time range, mean solar R.A., and objects present for all historic and planned future observations using the SPT-SZ, SPTpol, and SPT-3G cameras, constructed using the methods described in Section 3. We plot the results in Figure 7 and list details in Tables 3–5, respectively.

Table 3
Detections at 2.0 mm Predicted with SPT-SZ

Field Name	R.A. (°)	Decl. (°)	Time Range	Mean Solar R.A. (°)	Objects with Predicted S/N >3	Predicted S/N
RA5H30DEC-55	[75, 90]	[−60, −50]	2008 Feb 13–2008 Jun 5	19	⋯	⋯
RA5H30DEC-55	[75, 90]	[−60, −50]	2011 Jan 13–2011 Feb 20	314	⋯	⋯
RA5H30DEC-55	[75, 90]	[−60, −50]	2011 Aug 23–2011 Aug 24	152	⋯	⋯
RA5H30DEC-55	[75, 90]	[−60, −50]	2011 Sep 22–2011 Oct 4	184	⋯	⋯
RA5H30DEC-55	[75, 90]	[−60, −50]	2011 Oct 20–2011 Nov 13	216	⋯	⋯
RA23H30DEC-55	[345, 360]	[−60, −50]	2008 May 27–2008 Sep 25	125	⋯	⋯
RA23H30DEC-55	[345, 360]	[−60, −50]	2010 Apr 15–2010 May 13	36	⋯	⋯
RA21HDEC-60	[300, 330]	[−65, −55]	2009 Jan 31–2009 Jul 1	26	⋯	⋯
RA3H30DEC-60	[30, 75]	[−65, −55]	2009 Feb 4–2009 Mar 30	344	⋯	⋯
RA21HDEC-50	[300, 330]	[−55, −45]	2009 Jul 23–2009 Aug 10	131	(705) Erminia	8.4
RA21HDEC-50	[300, 330]	[−55, −45]	2009 Sep 1–2009 Nov 10	192	⋯	⋯
RA4H10DEC-50	[50, 75]	[−55, −45]	2010 Feb 3–2010 Apr 13	349	⋯	⋯
RA0H50DEC-50	[0, 25]	[−55, −45]	2010 May 13–2010 Jun 18	68	⋯	⋯
RA2H30DEC-50	[25, 50]	[−55, −45]	2010 Jun 19–2010 Jul 28	107	⋯	⋯
RA1HDEC-60	[0, 30]	[−65, −55]	2010 Jul 29–2010 Sep 11	149	⋯	⋯
RA5H30DEC-45	[75, 90]	[−50, −40]	2010 Oct 7–2010 Nov 5	206	⋯	⋯
RA6H30DEC-55	[90, 105]	[−60, −50]	2010 Oct 7–2010 Nov 13	210	⋯	⋯
RA6H30DEC-55	[90, 105]	[−60, −50]	2011 Mar 9–2011 Mar 23	355	⋯	⋯
RA6H30DEC-55	[90, 105]	[−60, −50]	2011 Jul 15–2011 Jul 17	115	⋯	⋯
RA23HDEC-62.5	[330, 360]	[−65, −60]	2010 Sep 12–2010 Oct 6	181	⋯	⋯
RA23HDEC-62.5	[330, 360]	[−65, −60]	2010 Apr 24–2010 Jul 15	72	⋯	⋯
RA21HDEC-42.5	[300, 330]	[−45, −40]	2010 Sep 12–2010 Oct 7	181	(31) Euphrosyne	20.1
					(154) Bertha	15.7
RA21HDEC-42.5	[300, 330]	[−45, −40]	2010 Apr 21–2010 Jul 14	70	⋯	⋯
RA22H30DEC-55	[330, 345]	[−60, −50]	2010 Sep 12–2010 Oct 5	180	⋯	⋯
RA22H30DEC-55	[330, 345]	[−60, −50]	2010 Apr 11–2010 Apr 21	24	⋯	⋯
RA22H30DEC-55	[330, 345]	[−60, −50]	2010 May 13–2010 Jul 10	79	⋯	⋯
RA23HDEC-45	[330, 360]	[−50, −40]	2010 Sep 12–2010 Oct 5	180	(31) Euphrosyne	13.3
					(772) Tanete	6.0
RA23HDEC-45	[330, 360]	[−50, −40]	2011 Mar 24–2011 Apr 11	11	⋯	⋯
RA23HDEC-45	[330, 360]	[−50, −40]	2011 May 13–2011 Jul 17	82	⋯	⋯
RA6HDEC-62.5	[75, 105]	[−65, −60]	2010 Sep 12–2010 Oct 7	181	⋯	⋯
RA6HDEC-62.5	[75, 105]	[−65, −60]	2011 Jan 11–2011 Feb 28	317	⋯	⋯
RA3H30DEC-42.5	[30, 75]	[−45, −40]	2010 Sep 12–2010 Oct 9	182	⋯	⋯
RA3H30DEC-42.5	[30, 75]	[−45, −40]	2011 Mar 1–2011 Mar 9	345	⋯	⋯
RA3H30DEC-42.5	[30, 75]	[−45, −40]	2011 Jul 17–2011 Aug 27	136	⋯	⋯
RA1HDEC-42.5	[0, 30]	[−45, −40]	2010 Sep 12–2010 Oct 6	181	⋯	⋯
RA1HDEC-42.5	[0, 30]	[−45, −40]	2011 Aug 28–2011 Sep 19	166	⋯	⋯
RA1HDEC-42.5	[0, 30]	[−45, −40]	2011 Oct 5–2011 Oct 8	192	⋯	⋯
RA6H30DEC-45	[90, 105]	[−50, −40]	2010 Sep 12–2010 Oct 3	179	⋯	⋯
RA6H30DEC-45	[90, 105]	[−50, −40]	2011 Sep 19–2011 Oct 28	194	⋯	⋯

Table 4
Detections at 2.0 mm Predicted with SPTpol

Field Name	R.A. (°)	Decl. (°)	Time Range	Mean Solar R.A. (°)	Objects with Predicted S/N >3	Predicted S/N
RA23H30DEC-55 (100d)	[345, 360]	[−60, −50]	2012 Feb 17–2012 Nov 21	103	⋯	⋯
RA23H30DEC-55 (100d)	[345, 360]	[−60, −50]	2013 Feb 8–2013 Apr 30	0	⋯	⋯
RA0HDEC-57.5 (500d)	[−30, 30]	[−65, −50]	2013 Apr 30–2013 Nov 27	141	⋯	⋯
RA0HDEC-57.5 (500d)	[−30, 30]	[−65, −50]	2014 Mar 25–2014 Dec 12	130	⋯	⋯
RA0HDEC-57.5 (500d)	[−30, 30]	[−65, −50]	2015 Mar 27–2015 Oct 26	109	(772) Tanete	6.9
RA0HDEC-57.5 (500d)	[−30, 30]	[−65, −50]	2016 Mar 23–2016 Sep 8	84	(326) Tamara	35.0
RA0P75HDEC-31 (KiDS)	[−30, 52.5]	[−36, −26]	2016 Sep 9–2016 Nov 15	198	(31) Euphrosyne	26.5
					(154) Bertha	11.3
					(451) Patientia	30.0
					(521) Brixia	12.3
					(532) Herculina	9.6
					(680) Genoveva	5.4
					(751) Faina	8.1
RA1HDEC-25	[0, 30]	[−30, −20]	2015 Dec 1–2016 Feb 1	280	⋯	⋯
RA1HDEC-35	[0, 30]	[−40, −30]	2014 Jan 12–2014 Feb 4	305	⋯	⋯
RA1HDEC-35	[0, 30]	[−40, −30]	2015 Dec 22–2015 Dec 23	270	⋯	⋯
RA3HDEC-25	[30, 60]	[−30, −20]	2014 Feb 22–2014 Mar 24	349	⋯	⋯
RA3HDEC-25	[30, 60]	[−30, −20]	2015 Feb 18–2015 Feb 27	335	⋯	⋯
RA3HDEC-35	[30, 60]	[−40, −30]	2014 Feb 4–2014 Feb 16	323	⋯	⋯
RA3HDEC-35	[30, 60]	[−40, −30]	2015 Feb 3–2015 Feb 23	326	⋯	⋯
RA5HDEC-25	[60, 90]	[−30, −20]	2015 Mar 1–2015 Mar 26	353	⋯	⋯
RA5HDEC-35	[60, 90]	[−40, −30]	2014 Feb 17–2014 Mar 7	339	⋯	⋯
RA5HDEC-35	[60, 90]	[−40, −30]	2015 Jan 22–2015 Jan 22	304	⋯	⋯
RA11HDEC-25	[150, 180]	[−30, −20]	2016 Jan 23–2016 Feb 12	315	⋯	⋯
RA11HDEC-25	[150, 180]	[−30, −20]	2016 Mar 7–2016 Mar 7	348	⋯	⋯
RA13HDEC-25	[180, 210]	[−30, −20]	2016 Feb 13–2016 Mar 22	344	(324) Bamberga[a]	16.3
					(382) Dodona	3.1
RA23HDEC-25	[330, 360]	[−30, −20]	2015 Oct 29–2015 Nov 29	255	(13) Egeria[a]	14.2
					(22) Kalliope[a]	13.2
RA23HDEC-35	[330, 360]	[−40, −30]	2013 Nov 27–2014 Jan 11	267	(164) Eva	6.5
RA23HDEC-35	[330, 360]	[−40, −30]	2015 Jan 26–2015 Feb 3	312	⋯	⋯

Note.
[a] Focus of this paper's analysis.

Table 5
Detections at 2.0 mm Predicted with SPT-3G

Field Name	R.A. (°)	Decl. (°)	Time Range	Mean Solar R.A. (°)	Objects with Predicted S/N >3	Predicted S/N
RA0HDEC-56 (1500d)	[−50, 50]	[−70, −42]	2019 Mar 21–2019 Dec 30	137	(413) Edburga	7.6
					(705) Erminia	21.3
RA0HDEC-56 (1500d)	[−50, 50]	[−70, −42]	2020 Mar 23–2020 Nov 25	122	(772) Tanete	14.3
					(1093) Freda	42.6
					(2906) Caltech	3.4
RA0HDEC-56 (1500d)	[−50, 50]	[−70, −42]	2021 Mar 1–2021 Dec 1	114	(31) Euphrosyne	57.0
					(344) Desiderata	123.1
					(814) Tauris	19.0
RA0HDEC-56 (1500d)[a]	[−50, 50]	[−70, −42]	2022 Mar 22–2022 Nov 30	123	⋯	⋯
RA0HDEC-56 (1500d)[a]	[−50, 50]	[−70, −42]	2023 Mar 22–2023 Nov 30	123	(247) Eukrate	18.6
					(323) Brucia	4.9
					(326) Tamara	40.6
					(350) Ornamenta	12.9
					(536) Merapi	9.3
					(617) Patroclus	4.0
RA5HDEC-45.5 (western)	[50, 100]	[−63, −28]	2020 Feb 10–2020 Mar 22	342	⋯	⋯
RA5HDEC-45.5 (western)[b]	[50, 100]	[−63, −28]	2021 Jan 12–2021 Feb 2	305	⋯	⋯
RA5HDEC-45.5 (western)	[50, 100]	[−63, −28]	2021 Dec 25–2022 Feb 13	300	⋯	⋯
RA5HDEC-45.5 (western)[a]	[50, 100]	[−63, −28]	2022 Dec 25–2023 Feb 13	300	(2) Pallas	214.6
RA1H40DEC-35 (mid-north)	[0, 50]	[−42, −28]	2020 Dec 1–2021 Jan 21	275	⋯	⋯
RA1H40DEC-35 (mid-north)	[0, 50]	[−42, −28]	2021 Nov 30–2022 Jan 2	264	⋯	⋯
RA1H40DEC-35 (mid-north)[a]	[0, 50]	[−42, −28]	2022 Dec 1–2022 Dec 24	259	⋯	⋯
RA12H30DEC-35 (backside)	[150, 225]	[−42, −28]	2021 Feb 3–2021 Mar 21	339	(480) Hansa	3.5
					(1266) Tone	4.0

Table 5
(Continued)

Field Name	R.A. (°)	Decl. (°)	Time Range	Mean Solar R.A. (°)	Objects with Predicted S/N >3	Predicted S/N
RA12H30DEC-35 (backside)	[150, 225]	[−42, −28]	2022 Feb 14–2022 Mar 21	344	(36) Atalante	6.4
					(445) Edna	3.4
					(773) Irmintraud	8.3
RA12H30DEC-35 (backside)[a]	[150, 225]	[−42, −28]	2023 Feb 14–2023 Mar 21	344	(426) Hippo	27.9
					(702) Alauda	11.0
					(705) Erminia	13.6
					(762) Pulcova	13.8

Notes.
[a] Planned future observations.
[b] Only the northernmost 7°.5 observed.

ORCID iDs

P. M. Chichura ● https://orcid.org/0000-0002-5397-9035
A. Foster ● https://orcid.org/0000-0002-7145-1824
M. Archipley ● https://orcid.org/0000-0002-0517-9842
B. A. Benson ● https://orcid.org/0000-0002-5108-6823
F. Bianchini ● https://orcid.org/0000-0003-4847-3483
L. E. Bleem ● https://orcid.org/0000-0001-7665-5079
F. R. Bouchet ● https://orcid.org/0000-0002-8051-2924
J.-F. Cliche ● https://orcid.org/0000-0001-6509-8430
T. M. Crawford ● https://orcid.org/0000-0001-9000-5013
M. A. Dobbs ● https://orcid.org/0000-0001-7166-6422
W. Everett ● https://orcid.org/0000-0002-5370-6651
S. Guns ● https://orcid.org/0000-0001-7143-2853
E. Hivon ● https://orcid.org/0000-0003-1880-2733
G. P. Holder ● https://orcid.org/0000-0002-0463-6394
M. Millea ● https://orcid.org/0000-0001-7317-0551
S. Patil ● https://orcid.org/0000-0001-5871-7520
K. A. Phadke ● https://orcid.org/0000-0001-7946-557X
C. M. Posada ● https://orcid.org/0000-0001-8810-096X
C. L. Reichardt ● https://orcid.org/0000-0003-2226-9169
B. Riedel ● https://orcid.org/0000-0002-9524-8943
G. Smecher ● https://orcid.org/0000-0002-5560-187X
J. A. Sobrin ● https://orcid.org/0000-0001-6155-5315
A. Springmann ● https://orcid.org/0000-0001-6401-0126
N. Whitehorn ● https://orcid.org/0000-0002-3157-0407
W. L. K. Wu ● https://orcid.org/0000-0001-5411-6920

References

Abazajian, K. N., Adshead, P., Ahmed, Z., et al. 2016, arXiv:610.02743
ALMA Partnership, et al. 2015, ApJL, 808, L2
Anderson, A. J., Ade, P. A. R., Ahmed, Z., et al. 2018, JLTP, 193, 1057
Austermann, J. E., Aird, K. A., Beall, J. A., et al. 2012, Proc. SPIE, 8452, 84521E
Bleem, L., Ade, P., Aird, K., et al. 2012, JLTP, 167, 859
Bleem, L. E., Bocquet, S., Stalder, B., et al. 2020, ApJS, 247, 25
Briggs, F. H. 1973, ApJ, 184, 637
Carlstrom, J. E., Ade, P. A. R., Aird, K. A., et al. 2011, PASP, 123, 568
Conklin, E. K., Ulich, B. L., Dickel, J. R., & Ther, D. T. 1977, in IAU Colloq. 39: Comets, Asteroids, Meteorites, ed. A. H. Delsemme (Toledo, OH: Univ. Toledo), 257
Cremonese, G., Marzari, F., Burigana, C., & Maris, M. 2002, NewA, 7, 483
de Kleer, K., Cambioni, S., & Shepard, M. 2021, PSJ, 2, 149
Delbó, M., & Harris, A. 2002, M&PS, 37, 1929
Descamps, P., Marchis, F., Pollock, J., et al. 2008, Icar, 196, 578
Ďurech, J., Kaasalainen, M., Herald, D., et al. 2011, Icar, 214, 652
Ďurech, J., Sidorin, V., & Kaasalainen, M. 2010, A&A, 513, A46
Everett, W. B., Zhang, L., Crawford, T. M., et al. 2020, ApJ, 900, 55
Ginsburg, A., Sipőcz, B. M., Brasseur, C. E., et al. 2019, AJ, 157, 98
Giorgini, J. 2020, DASTCOM5: JPL small-body data browser, Astrophysics Source Code Library, ascl:2009.023
Giorgini, J. D., Yeomans, D. K., Chamberlin, A. B., et al. 1996, AAS Meeting, 28, 25.04
Gulkis, S., Keihm, S., Kamp, L., et al. 2012, P&SS, 66, 31
Guns, S., Foster, A., Daley, C., et al. 2021, ApJ, 916, 98
Hanuš, J., Viikinkoski, M., Marchis, F., et al. 2017, A&A, 601, A114
Harris, A. 1998, Icar, 131, 291
Henning, J. W., Sayre, J. T., Reichardt, C. L., et al. 2018, ApJ, 852, 97
Johnston, K., Seidelmann, P., & Wade, C. 1982, AJ, 87, 1593
Kaasalainen, M., Torppa, J., & Piironen, J. 2002, Icar, 159, 369
Keihm, S., Kamp, L., Gulkis, S., et al. 2013, Icar, 226, 1086
Keihm, S., Tosi, F., Kamp, L., et al. 2012, Icar, 221, 395
Kosowsky, A. 2003, in Proc. Workshop: The Cosmic Microwave Background and its Polarization, New Astronomy Reviews, ed. S. Hanany & K. A. Olive (Amsterdam: Elsevier)
Lagerros, J. S. V. 1996, A&A, 315, 625
Lebofsky, L. A., & Spencer, J. R. 1989 in Asteroids II: Proc. Conf. Radiometry and thermal modeling of asteroids. ed. R. P. Binzel, T. Gehrels, & M. S. Matthews (Tucson, AZ: Univ. Arizona Press), 128
Lebofsky, L. A., Sykes, M. V., Tedesco, E. F., et al. 1986, Icar, 68, 239
Lellouch, E., Moreno, R., Müller, T., et al. 2017, A&A, 608, A45
Levison, H. F., Olkin, C. B., Noll, K. S., et al. 2021, PSJ, 2, 171
Li, J.-Y., Moullet, A., Titus, T. N., Hsieh, H. H., & Sykes, M. V. 2020, AJ, 159, 215
Magri, C., Nolan, M. C., Ostro, S. J., & Giorgini, J. D. 2007, Icar, 186, 126
Mainzer, A., Bauer, J., Cutri, R., et al. 2019, PDSS
Mainzer, A., Bauer, J., Grav, T., et al. 2011, ApJ, 731, 53
Marchis, F., Enriquez, J. E., Emery, J. P., et al. 2012, Icar, 221, 1130
Margot, J., & Brown, M. 2003, Sci, 300, 1939
Masiero, J. R., Grav, T., Mainzer, A. K., et al. 2014, ApJ, 791, 121
Michel, P., DeMeo, F. E., & Bottke, W. F. 2015, in Asteroids IV, ed. P. Michel, F. E. DeMeo, & W. F. Bottke (Tucson, AZ: Univ. Arizona Press), 3
Moullet, A., Gurwell, M., & Carry, B. 2010, A&A, 516, L10
Müller, T. G., & Barnes, P. J. 2007, A&A, 467, 737
Murphy, T., Sadler, E. M., Ekers, R. D., et al. 2010, MNRAS, 402, 2403
Naess, S., Aiola, S., Battaglia, N., et al. 2021, ApJ, 923, 224
Nugent, C. R., Mainzer, A., Masiero, J., et al. 2015, ApJ, 814, 117
Opeil, C. P., Consolmagno, G. J., & Britt, D. T. 2010, Icar, 208, 449
Padin, S., Staniszewski, Z., Keisler, R., et al. 2008, ApOpt, 47, 4418
Planck Collaboration, Adam, R., Ade, P. A. R., et al. 2016, A&A, 594, A10
Planck Collaboration, Ade, P. A. R., Aghanim, N., et al. 2014, A&A, 571, A14
Redman, R., Feldman, P., Matthews, H., Halliday, I., & Creutzberg, F. 1992, AJ, 104, 405
Shepard, M. K., Taylor, P. A., Nolan, M. C., et al. 2015, Icar, 245, 38
Simons Observatory Collaboration, et al. 2019, JCAP, 2019, 056
Sobrin, J. A., Anderson, A. J., Bender, A. N., et al. 2022, ApJS, 258, 42
Spencer, J., Lebofsky, L., & Sykes, M. 1989, Icar, 78, 337
Ulich, B., & Conklin, E. 1976, Icar, 27, 183
VanderPlas, J. T. 2018, ApJS, 236, 16
Vernazza, P., Ferrais, M., Jorda, L., et al. 2021, A&A, 654, A56
Virkki, A., Muinonen, K., & Penttilä, A. 2014, M&PS, 49, 86
Warner, B., Harris, A., & Pravec, P. 2009, Icar, 202, 134
Webster, W., Johnston, K., Hobbs, R., et al. 1988, AJ, 95, 1263